The Discontinuity-Enriched Finite Element Method

Aragón, Alejandro M.; Simone, Angelo

Important note
To cite this publication, please use the final published version (if applicable).
Please check the document version above.

WILEY

The Discontinuity-Enriched Finite Element Method

Alejandro M. Aragón[1] | Angelo Simone[2]

[1]Faculty of Mechanical, Maritime and Materials Engineering, Delft University of Technology, Mekelweg 2, 2628 CD Delft, The Netherlands

[2]Faculty of Civil Engineering and Geosciences, Delft University of Technology, Stevinweg 1, 2628 CN Delft, The Netherlands

Correspondence
Alejandro M. Aragón, Department of Precision and Microsystems Engineering, Faculty of 3mE, Delft University of Technology, Mekelweg 2, 2628 CD Delft, The Netherlands.
Email: a.m.aragon@tudelft.nl

Summary

We introduce a new methodology for modeling problems with both weak and strong discontinuities independently of the finite element discretization. At variance with the eXtended/Generalized Finite Element Method (X/GFEM), the new method, named the Discontinuity-Enriched Finite Element Method (DE-FEM), adds enriched degrees of freedom only to nodes created at the intersection between a discontinuity and edges of elements in the mesh. Although general, the method is demonstrated in the context of fracture mechanics, and its versatility is illustrated with a set of traction-free and cohesive crack examples. We show that DE-FEM recovers the same rate of convergence as the standard FEM with matching meshes, and we also compare the new approach to X/GFEM.

KEYWORDS

cohesive cracks, fracture mechanics, GFEM, IGFEM, strong discontinuities, XFEM

1 | INTRODUCTION

This article is concerned with problems whose solution is C^0– and C^{-1}–continuous, *i.e.*, problems containing weak and strong discontinuities, respectively. The eXtended/Generalized Finite Element Method (X/GFEM) has revolutionized the modeling of such discontinuities. The most significant asset of X/GFEM is the capability to decouple the representation of a discontinuity from the underlying finite element discretization. Here, we introduce a novel discontinuity-enriched finite element formulation that has several advantages with respect to X/GFEM. This approach promises a new modeling paradigm by placing enriched nodes only along discontinuities. This has important implications in terms of computer implementation and, in particular, in the imposition of Dirichlet boundary conditions.

The standard Finite Element Method (FEM) has been traditionally used to model weak and strong discontinuities by designing *conforming* or *matching* meshes in which the edges of finite elements align to such discontinuities. For weak discontinuities, the jump in the field gradient is readily accommodated by the C^0 continuity at finite element edges. Strong discontinuities such as cracks require the definition of so-called double nodes along edges of finite elements aligned with the crack geometry. To date, the creation of matching discretizations remains an error-prone process that can even result in an inadequate mesh because finite elements with bad aspect ratios can be a source of large numerical errors. Creating matching meshes also requires the use of robust (and expensive) software. Furthermore, modeling problems with evolving geometries or discontinuities renders the cost of creating such a matching mesh prohibitive (specially in 3-D simulations).

X/GFEM[1,2] tackles such problems in an elegant manner as discontinuities need not conform to the finite element mesh. This flexibility in the analysis, however, comes at a price because the complexity of the conformal mesh generation is transferred

to that of the detection of the intersection between elements and a discontinuity, and to related subsidiary implementations. Nevertheless, X/GFEM has proven to outmatch the standard FEM in problems with evolving geometric features such as crack propagation,[1] moving interfaces,[3] topology optimization,[4] and phase/solidification problems.[5] Despite these undeniable advantages, X/GFEM suffers from shortcomings that are either rooted in its theoretical background (the need to enrich all nodes in elements crossed by a discontinuity) or whose solution is still not definitive (the high condition number issue[6,7]).

Similar to X/GFEM, the Interface-enriched Generalized Finite Element Method (IGFEM)[8] relies on enriched nodes to improve the local approximation. Unlike X/GFEM, enriched nodes are generated along the discontinuity, at the intersection with element edges. IGFEM was introduced to model weak discontinuities of the type encountered in multiphase materials with perfectly bonded interfaces. IGFEM proved not only to be optimally convergent but also easier to implement than X/GFEM. Since its introduction, the method has been improved to handle multiple interfaces crossing a single finite element[9] and to reduce the discretization error of curved interfaces.[10] Moreover, it has also been used in a wide range of applications, including the damage response of heterogeneous adhesives,[11] the modeling of microvascular actively cooled materials,[8,12] woven composites,[9,12] and pitting corrosion.[13] More recently, the mesh independence capability of IGFEM has been extended to treat external boundaries by Cuba-Ramos *et al.*,[14] positioning the method as an *immerse boundary* technique. The formulation proposed in that work solves a major nuisance of X/GFEM, for it solves the fundamental issue of artificial oscillations in the traction field while imposing essential (Dirichlet) boundary conditions on an external nonconforming boundary.[15]

Here, building upon IGFEM, we introduce the Discontinuity-Enriched Finite Element Method (DE-FEM) for modeling both weak and strong discontinuities. By adding a properly designed discontinuous enrichment function, the resulting method is able to handle also strong discontinuities and inherits the same advantages of IGFEM with respect to X/GFEM. Finally, we show that DE-FEM performs remarkably better than X/GFEM in modeling rigid cohesive cracks, where the latter has been shown to poorly represent the cohesive traction profile.[16]

As mentioned earlier, the new method can be used to model both weak and strong discontinuities. Yet, since much research has been conducted on IGFEM, this article focuses only on strong discontinuities. In this regard, even though emphasis is placed on fracture mechanics, the formulation is general and can be used to solve other problems where strong discontinuities are encountered. Without compromising on either accuracy or efficiency, the new formulation is also more straightforward to implement than X/GFEM.

2 | FORMULATION

The method is first demonstrated by means of a one-dimensional problem whose solution is contrasted to that obtained with X/GFEM. A formal formulation for higher dimensions is given in Section 2.2.

2.1 | A 1-D example with both weak and strong discontinuities

Figure 1 shows a 1-D bar of length L clamped at the left end and subjected to a load P at the right end. The bar is composed by two parts, Ω_I and Ω_{II}, that are connected at $x = x_\Gamma$ by an elastic spring of stiffness k. In addition to the strong discontinuity at x_Γ, the mismatch in Young's modulus between the parts also introduces a weak discontinuity. The solution of the corresponding boundary value problem yields the displacement at the free end expressed as the sum of the elastic deformation contributions of the parts and the spring:

$$u(L) = \frac{PwL}{E_I A} + \frac{P}{k} + \frac{P(1-w)L}{E_{II} A}, \tag{1}$$

where $w = x_\Gamma/L$ is the location of the discontinuity relative to the length of the bar.
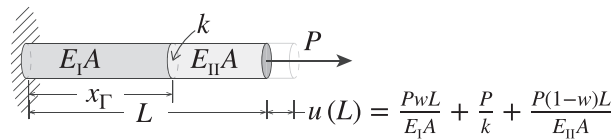

FIGURE 1 Clamped bar subjected to a load P and composed of two parts of length wL and $(1-w)L$, with $w = x_\Gamma/L$, connected by a spring of stiffness k. The parts have axial stiffness $E_I A$ and $E_{II} A$ at the left- and right-hand side, respectively, of a discontinuity at x_Γ. The figure also shows the exact displacement at the free end.

We now solve the problem with a single finite element, denoted Ω, employing a solution of the form

$$u^h(x) = \underbrace{\sum_{j=1}^{2} N_j(x)U_j}_{\text{std. FEM}} + \underbrace{\underbrace{\psi(x)\alpha}_{\text{weak}} + \underbrace{\chi(x)\beta}_{\text{strong}}}_{\text{enriched}}. \tag{2}$$

One may immediately recognize that Equation (2) shows a structure similar to that of X/GFEM. The first term corresponds to the standard FEM component of the approximation, where the Lagrange shape functions N_j and the standard degrees of freedom (DOFs) U_j are associated with the end nodes (those identified with the ● symbol in Figure 2A). The other terms enrich the approximation. The functions ψ and χ are enrichment functions for a weak and a strong discontinuity, respectively, and α and β are their corresponding enriched DOFs. These enrichment functions are created from Lagrange shape functions in sub-domains Ω_I, Ω_{II} (see Figure 2B). In Equation (2), ψ is the IGFEM enrichment function that is used to introduce a jump in the gradient of the field.[8,10] For this simple example, we will just use

$$\psi = \begin{cases} N_{i^-}^I(x) & \text{for } x < x_\Gamma \\ N_{i^+}^{II}(x) & \text{for } x > x_\Gamma \end{cases}. \tag{3}$$

Therefore, the weak enrichment attains a maximum value of one at x_Γ, and it ramps linearly to zero at the ends of the bar. Note that the IGFEM weak enrichment uses a scale factor to improve the conditioning as the interface is moved closer to a node;[10] to ease the presentation, such scaling is omitted here.

The information about the discontinuous field, here understood as a kinematic enrichment, is incorporated in χ. To construct this enrichment, we seek to satisfy the following two conditions:

1. In the spirit of IGFEM,[8] the enrichment function is created through a linear combination of Lagrange shape functions in sub-domains or *integration elements*, i.e., elements Ω_I, Ω_{II} created to the left and right side of the discontinuity; and

2. we require a jump of unit magnitude, i.e., $[\![\chi]\!] = \chi|_{x_\Gamma^+} - \chi|_{x_\Gamma^-} = 1$. By ensuring this condition, the enriched DOF β in Equation (2) represents the jump in the displacement field at $x = x_\Gamma$, thus attributing an immediate physical interpretation to the enriched DOF.
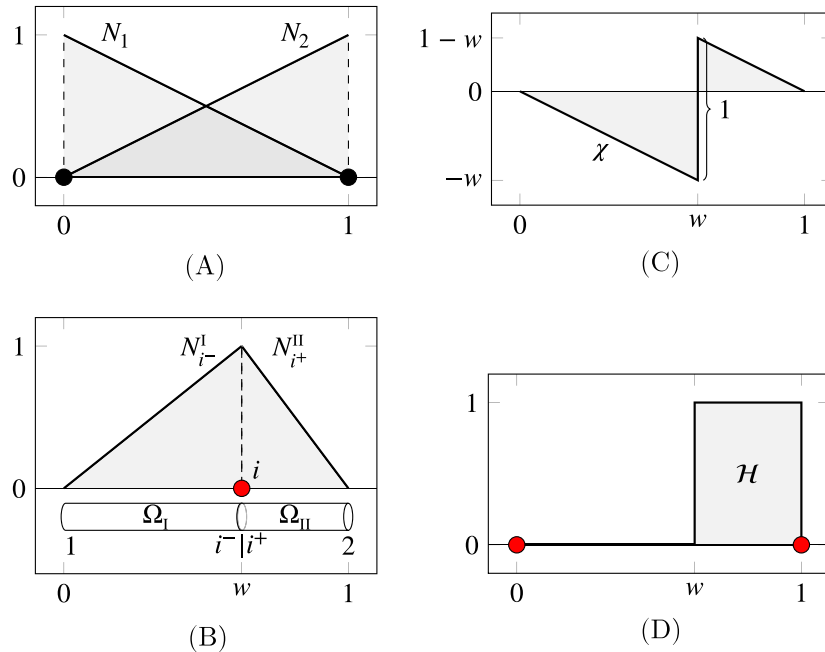
FIGURE 2 (A) Lagrange shape functions for standard FEM associated with standard DOFs (●); (B) sub-domains Ω_I and Ω_{II} are created with the aid of a new node i that is associated with enriched DOFs α and β (●). The figure also shows the Lagrange shape functions in these sub-domains that are used to create weak (ψ) and strong (χ) enrichment functions; (C) strong discontinuity enrichment function χ associated to DOF β, showing a unit jump at $x/L = w$; and (D) Heaviside step function $\mathcal{H}$ used in X/GFEM and additional enriched DOFs (●).

The first condition can be expressed as

$$
\chi = \begin{cases} w_1 N^{\mathrm{I}}_{i-}(x) & \text{for } x < x_\Gamma \\ w_2 N^{\mathrm{II}}_{i+}(x) & \text{for } x > x_\Gamma \end{cases}, \tag{4}
$$

where w_1 and w_2 are still unknown weights, and, as shown in Figure 2B, $N^{\mathrm{I}}_{i-}(x) = x/x_\Gamma$ and $N^{\mathrm{II}}_{i+}(x) = (L-x)/(L-x_\Gamma)$. To satisfy the second condition, we remark that the Lagrange shape functions N_j form a *partition of unity*, i.e., $\sum_j N_j = 1$. By noting that $|\mp N_1 - (\pm N_2)| = 1$, $\forall x \in \Omega$, the weights are obtained from

$$
w_1 N^{\mathrm{I}}_{i-}(x_\Gamma) = -N_2(x_\Gamma) \quad \text{and} \tag{5}
$$

$$
w_2 N^{\mathrm{II}}_{i+}(x_\Gamma) = N_1(x_\Gamma). \tag{6}
$$

Equation (5) yields $w_1 = -x_\Gamma/L = -w$ while Equation (6) yields $w_2 = 1 + w_1 = 1 - w$. Thus, the enrichment function shown in Figure 2C takes the final form

$$
\chi = \begin{cases} -w\dfrac{x}{x_\Gamma} & \text{for } x < x_\Gamma \\ (1-w)\dfrac{L-x}{L-x_\Gamma} & \text{for } x > x_\Gamma \end{cases}. \tag{7}
$$

Equation (7) can be interpreted as having the Lagrange shape functions (associated with the discontinuity location) in integration elements being weighted by the location of the discontinuity relative to the length. Observe that, even though Equation (7) seems to degenerate as $x_\Gamma \to 0$ or $x_\Gamma \to L$, the enrichment function is bounded. In fact, noting that $w = x_\Gamma/L$, we find that $\lim_{x_\Gamma \to 0} \chi = N_1$, $\lim_{x_\Gamma \to L} \chi = -N_2$.

Having determined the discontinuous enrichment, we can now proceed with the solution of this problem following standard procedures. Defining $N = \begin{bmatrix} N_1 & N_2 & \psi & \chi \end{bmatrix}$, $B(x) = \mathrm{d}N/\mathrm{d}x$, and $M = \begin{bmatrix} 0 & 0 & 0 & 1 \end{bmatrix}$, the stiffness matrix and force vector are given by

$$
K = \int_0^{x_\Gamma} E_{\mathrm{I}} A\, B^{\mathsf{T}} B\, \mathrm{d}x + \int_{x_\Gamma}^{L} E_{\mathrm{II}} A\, B^{\mathsf{T}} B\, \mathrm{d}x + k M^{\mathsf{T}} M
$$

$$
= \frac{A}{L} \left[\begin{array}{c:ccc}
E_{\mathrm{II}} - w\,\llbracket E \rrbracket & -E_{\mathrm{II}} + w\,\llbracket E \rrbracket & \llbracket E \rrbracket & E_{\mathrm{II}} - w\,\llbracket E \rrbracket \\ \hdashline
-E_{\mathrm{II}} + w\,\llbracket E \rrbracket & E_{\mathrm{II}} - w\,\llbracket E \rrbracket & -\llbracket E \rrbracket & -E_{\mathrm{II}} + w\,\llbracket E \rrbracket \\
\llbracket E \rrbracket & -\llbracket E \rrbracket & \dfrac{E_{\mathrm{I}}}{w} + \dfrac{E_{\mathrm{II}}}{1-w} & \llbracket E \rrbracket \\
E_{\mathrm{II}} - w\,\llbracket E \rrbracket & -E_{\mathrm{II}} + w\,\llbracket E \rrbracket & \llbracket E \rrbracket & E_{\mathrm{II}} - w\,\llbracket E \rrbracket + \dfrac{kL}{A}
\end{array} \right] \quad \text{and} \quad F = \begin{bmatrix} R \\ -P \\ 0 \\ 0 \end{bmatrix}, \tag{8}
$$

respectively, where $\llbracket E \rrbracket \equiv E_{\mathrm{II}} - E_{\mathrm{I}}$. It is worth noting that both weak and strong enrichment functions are equal to zero at the left end; therefore, imposing the essential boundary condition, i.e., $u(0) = 0$, is as straightforward as in the standard FEM. The system $KU = F$ has solution

$$
U = \left[0 \quad \frac{PwL}{E_{\mathrm{I}} A} + \frac{P}{k} \quad \frac{P(1-w)L}{E_{\mathrm{II}} A} \quad \frac{\llbracket E \rrbracket Pw(1-w)L}{E_{\mathrm{I}} E_{\mathrm{II}} A} \quad \frac{P}{k} \right]^{\mathsf{T}}, \tag{9}
$$

and thus, the approximation recovers the exact displacement field

$$
u^h(x) = \begin{cases} \dfrac{P}{E_{\mathrm{I}} A} x & \text{for } x < x_\Gamma \\ \dfrac{PwL}{E_{\mathrm{I}} A} + \dfrac{P}{k} + \dfrac{P(x/L - w)L}{E_{\mathrm{II}} A} & \text{for } x > x_\Gamma \end{cases}. \tag{10}
$$

We can infer the following by inspecting Equation (9):

- when $E_{\mathrm{II}} = E_{\mathrm{I}} = E$, the solution simplifies to

$$U = \left[0 \quad \frac{PL}{EA} + \frac{P}{k} \quad 0 \quad \frac{P}{k} \right]^{\mathsf{T}}, \tag{11}$$

with an inactive weak enrichment;

- the perfectly bonded case is recovered when $k \to \infty$, the solution becomes

$$U = \left[0 \quad \frac{PwL}{E_{\mathrm{I}}A} + \frac{P(1-w)L}{E_{\mathrm{II}}A} \quad \frac{[\![E]\!]Pw(1-w)L}{E_{\mathrm{I}}E_{\mathrm{II}}A} \quad 0 \right]^{\mathsf{T}}, \tag{12}$$

with an inactive strong enrichment; and

- when both conditions $E_{\mathrm{II}} = E_{\mathrm{I}} = E$ and $k \to \infty$ are met (perfectly bonded parts of the same material), the solution vector is

$$U = \left[0 \quad \frac{PL}{EA} \quad 0 \quad 0 \right]^{\mathsf{T}}, \tag{13}$$

and both weak and strong enrichments are inactive.

We would like to stress that an independent linear field at each side of x_{Γ} can only be obtained by using both weak and strong enrichments. In other words, using the strong discontinuity enrichment χ alone would fail to produce two independent linear fields because $\mathrm{d}\chi/\mathrm{d}x$ is the same at either side of the discontinuity.

We now turn our attention to the solution obtained with X/GFEM, where we use the Heaviside step function in Figure 2D,

$$\mathcal{H} = \begin{cases} 0 \text{ for } x < x_{\Gamma} \\ 1 \text{ for } x > x_{\Gamma} \end{cases}, \tag{14}$$

as enrichment. This enrichment, equal to zero at the left end of the bar, has been chosen to simplify the enforcement of the essential boundary condition; therefore, as in standard FEM, this relates to the standard DOF only. A step function with a value different from zero at the clamped boundary would have required the enforcement of a multi freedom constraint through master-slave elimination, Lagrange multiplier adjunction, or penalty augmentation,[17,18] as the displacement field is now a function of both standard and enriched DOFs. This is at variance with DE-FEM, where the enrichment function is always zero at standard mesh nodes; this implies that standard FEM procedures can *always* be used in DE-FEM to enforce Dirichlet boundary conditions.

The bar is again discretized with a single finite element, and the vector of nodal unknowns contains the standard DOFs followed by those corresponding to the enrichment function. The stiffness matrix and the force vector are expressed as

$$K = \frac{A}{L} \begin{bmatrix} E_{\mathrm{II}} - w[\![E]\!] & -E_{\mathrm{II}} + w[\![E]\!] & E_{\mathrm{II}}(1-w) & -E_{\mathrm{II}}(1-w) \\ -E_{\mathrm{II}} + w[\![E]\!] & E_{\mathrm{II}} - w[\![E]\!] & -E_{\mathrm{II}}(1-w) & E_{\mathrm{II}}(1-w) \\ E_{\mathrm{II}}(1-w) & -E_{\mathrm{II}}(1-w) & \dfrac{(w-1)(kL(w-1)-AE_{\mathrm{II}})}{A} & \dfrac{(w-1)(AE_{\mathrm{II}}-kLw)}{A} \\ -E_{\mathrm{II}}(1-w) & E_{\mathrm{II}}(1-w) & \dfrac{(w-1)(AE_{\mathrm{II}}-kLw)}{A} & E_{\mathrm{II}}(1-w) + \dfrac{kLw^2}{A} \end{bmatrix} \tag{15}$$

and

$$F = \begin{bmatrix} R & P & 0 & P \end{bmatrix}^{\mathsf{T}}. \tag{16}$$

The system $KU = F$ has solution

$$U = \left[0 \quad \frac{PL}{E_{\mathrm{I}}A} \quad \frac{P}{k} + \frac{[\![E]\!]PwL}{E_{\mathrm{I}}E_{\mathrm{II}}A} \quad \frac{P}{k} + \frac{[\![E]\!]P(w-1)L}{E_{\mathrm{I}}E_{\mathrm{II}}A} \right]^{\mathsf{T}}, \tag{17}$$

yielding the same displacement field as in Equation (10).

2.2 | Formulation in higher dimensions

Consider the Euclidean vector space $\mathbb{R}^d$ ($d = 2, 3$) spanned by an orthonormal basis $\{e_i\}$. A solid body (*cf.* Figure 3 for the 2-D case) is represented by the open domain $\Omega \subset \mathbb{R}^d$ bounded by $\Gamma \equiv \partial\Omega = \overline{\Omega} \setminus \Omega$ with outer unit normal n_{Γ}. The boundary
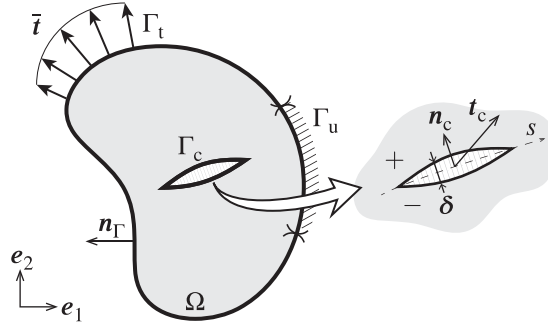
FIGURE 3 Conventions for a body Ω with a cohesive crack Γ_c. The boundaries Γ_u and Γ_t represent portions of the boundary Γ (with outer unit normal $\boldsymbol{n}_\Gamma$) with prescribed Dirichlet and Neumann boundary conditions, respectively. The inset shows a cohesive crack parameterized by the curve s.

Γ is, in turn, subdivided into two disjoint regions, $\Gamma_u \neq \emptyset$ and Γ_t, where essential (Dirichlet) and natural (Neumann) boundary conditions are prescribed, respectively. Consider a crack $\Gamma_c \subseteq \Gamma_t$ parameterized by a coordinate s along which a displacement jump $\boldsymbol{\delta} \equiv [\![\boldsymbol{u}]\!] \; \forall \boldsymbol{x} \in \Gamma_c$ is defined. The two regions adjacent to the crack are conveniently labeled as *positive* and *negative* as shown in Figure 3. To uniquely label these domains, the crack is endowed with a direction given by the unit vector $\boldsymbol{n}_c$ normal to the crack. Given a point $\boldsymbol{p} \in \Omega$, let $\boldsymbol{y} = \arg\min_{\boldsymbol{x} \in \Gamma_c} \|\boldsymbol{x} - \boldsymbol{p}\|$ be the closest point on the crack. Point $\boldsymbol{p}$ lies on the positive side if $\boldsymbol{n}_c \cdot (\boldsymbol{p} - \boldsymbol{y}) > 0$, where $\boldsymbol{n}_c$ is evaluated at point $\boldsymbol{y}$.

Consider now the vector-valued function spaces

$$\mathcal{V}(\Omega) = \left\{ \boldsymbol{v} : \boldsymbol{v}(\boldsymbol{x}) \in \mathbb{R}^d \; \forall \boldsymbol{x} \in \Omega; \; v_i \in H^1(\Omega), i = 1, \dots, d \right\},$$
$$\mathcal{V}_0(\Omega) = \left\{ \boldsymbol{v} \in \mathcal{V}(\Omega) : \; \boldsymbol{v}|_{\Gamma_u} = \boldsymbol{0} \right\}, \tag{18}$$

where $H^1(\Omega)$ denotes the first-order Sobolev function space on Ω. Taking $\tilde{\boldsymbol{u}} \in \mathcal{V} : \; \tilde{\boldsymbol{u}}|_{\Gamma_u} = \bar{\boldsymbol{u}}$, we define the linear variety $\mathcal{V}^\star \equiv \tilde{\boldsymbol{u}} + \mathcal{V}_0$ so that every element in $\mathcal{V}^\star$ satisfies the Dirichlet boundary condition. The weak form of the static boundary value problem for a deformable cracked body is expressed as:

Given the prescribed displacement $\bar{\boldsymbol{u}} : \Gamma_u \to \mathbb{R}^d$, the prescribed traction $\bar{\boldsymbol{t}} : \Gamma_t \setminus \Gamma_c \to \mathbb{R}^d$, the cohesive traction $\boldsymbol{t}_c : \Gamma_c \to \mathbb{R}^d$, the Cauchy stress $\boldsymbol{\sigma} : \overline{\Omega} \times \overline{\Omega} \to \mathbb{R}^d$, and the body force $\boldsymbol{b} : \Omega \to \mathbb{R}^d$, find the displacement field $\boldsymbol{u} \in \mathcal{V}^\star$ such that

$$\int_\Omega \boldsymbol{\sigma}(\boldsymbol{u}) : \boldsymbol{\varepsilon}(\boldsymbol{v}) \, d\Omega = \int_\Omega \boldsymbol{v} \cdot \boldsymbol{b} \, d\Omega + \int_{\Gamma_t} \boldsymbol{v} \cdot \bar{\boldsymbol{t}} \, d\Gamma + \int_{\Gamma_c} [\![\boldsymbol{v}]\!] \cdot \boldsymbol{t}_c \, d\Gamma \quad \forall \boldsymbol{v} \in \mathcal{V}_0, \tag{19}$$

where $\boldsymbol{\varepsilon} \equiv \frac{1}{2}(\boldsymbol{\nabla}\boldsymbol{v} + \boldsymbol{\nabla}\boldsymbol{v}^\mathsf{T})$.

To solve this equation, the domain is discretized into a series of finite elements Ω_i that are not conforming to the crack, such that $\Omega^h = \text{int}\left(\cup_i \overline{\Omega}_i\right) \approx \Omega$ and $\Omega_i \cap \Omega_j = \emptyset, i \neq j$.

The functions $\boldsymbol{u}^h$ that are used in the finite-dimensional form of Equation (19) have to be chosen from a set that allows for a displacement jump at Γ_c. In DE-FEM, the displacement field takes the form

$$\boldsymbol{u}^h(\boldsymbol{x}) = \underbrace{\sum_{i \in \iota_h} N_i(\boldsymbol{x}) \boldsymbol{U}_i}_{\text{std. FEM}} + \underbrace{\sum_{i \in \iota_w} \psi_i(\boldsymbol{x}) \boldsymbol{\alpha}_i}_{\text{weak}} + \underbrace{\sum_{i \in \iota_s} \chi_i(\boldsymbol{x}) \boldsymbol{\beta}_i}_{\text{strong}}. \tag{20}$$

In the first term, ι_h is the index set of standard FEM nodes, N_i denotes the ith Lagrange shape function, and $\boldsymbol{U}_i$ is the vector of corresponding DOFs. In the second and third terms, which represent the enriched portion of the approximation, ι_w and ι_s denote index sets of nodes associated with weak ($\boldsymbol{\alpha}_i$) and strong ($\boldsymbol{\beta}_i$) enriched DOFs. The corresponding enrichment functions for weak and strong discontinuities are ψ_i and χ_i, respectively. These enrichment functions are constructed by the combination of Lagrange shape functions in elements (the so-called integration elements) that are created by partitioning the mesh element intersected by a discontinuity. These functions are local to their parent elements by construction, and thus the multiplication by the partition of unity of the underlying mesh is not required as it is done with X/GFEM. Figure 4 shows a schematic representation of (A) DE-FEM and (B) X/GFEM discretizations, where elements that interact with the crack are darker and additional DOFs are added to locations marked with the ● symbol. Note that enriched DOFs in DE-FEM are assigned to new
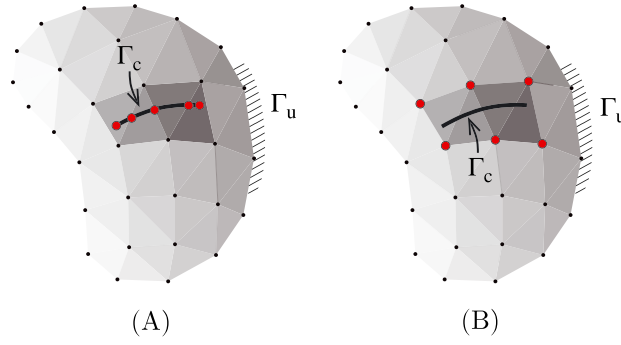
FIGURE 4 (A) DE-FEM and (B) X/GFEM discretizations showing in darker shade the elements traversed by the crack Γ_c and enriched nodes (●).
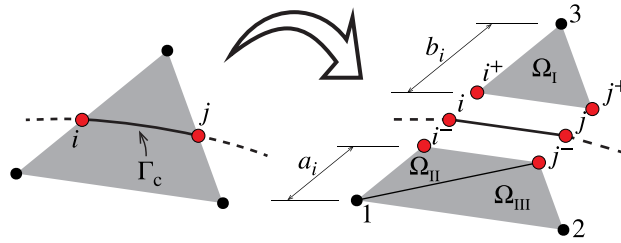

FIGURE 5 Integration elements used for the construction of DE-FEM discontinuous enrichment functions. These elements are defined with the aid of nodes i, j that are created at locations where a crack Γ_c intersects the edges of a three-node triangular element.

nodes created along the crack instead to those of the original mesh. In what follows, we will focus on the construction of the strong discontinuity enrichment, although a similar reasoning can be applied to the construction of weak enrichments; the latter follows previous studies[8,10] and will not be reported here.

For the construction of the strong discontinuity enrichment for 2-D elements, we consider the three-node triangular element shown in Figure 5. The strong discontinuity Γ_c intersects the element edges at locations where we create the new nodes i and j, to which we associate enriched DOFs β_i and β_j, respectively. We identify the node with a plus (minus) sign superscript when it is considered as part of the positive (negative) side of the discontinuity. These newly created nodes are used to identify the integration elements Ω_I, Ω_{II}, and Ω_{III} shown in Figure 5. The objective is now to determine the strong enrichment function by obtaining the weights that are associated with nodes i and j. Following the same procedure described in Section 2.1, the equations

$$w_{i1} N_{i+}^{I}(\boldsymbol{x}_i) = -N_3(\boldsymbol{x}_i) \text{ and} \tag{21}$$

$$w_{i2} N_{i-}^{II}(\boldsymbol{x}_i) = N_1(\boldsymbol{x}_i) \tag{22}$$

are used to determine w_{i1}, w_{i2}. Next, we define $w_i = -w_{i1}$ so that $w_{i2} = 1 - w_i$. It is worth noting that the weight is bounded, *i.e.*, $0 \leqslant w_i \leqslant 1$. It can be shown that obtaining the weight w_i in this way is equivalent to computing $w_i = a_i/(a_i + b_i)$, where a_i and b_i (*cf.* Figure 5) are the lengths of the sides of the integration elements Ω_{II} and Ω_I, respectively. Once the weight is determined, the discontinuous enrichment function associated with β_i is

$$\chi_i = \begin{cases} -w_i N_{i+}^{I}(\boldsymbol{x}) & \text{for } \boldsymbol{x} \in \Omega_I \\ (1 - w_i) N_{i-}^{II}(\boldsymbol{x}) & \text{for } \boldsymbol{x} \in \Omega_{II} \end{cases}. \tag{23}$$

Similarly, for the jth node, the equations

$$w_{j1} N_{j+}^{I}(\boldsymbol{x}_j) = -N_3(\boldsymbol{x}_j) \text{ and} \tag{24}$$

$$w_{j2} N_{j-}^{III}(\boldsymbol{x}_j) = N_2(\boldsymbol{x}_j) \tag{25}$$

determine w_{j1}, w_{j2} so that $w_j = -w_{j1}$ and $0 \leqslant w_j \leqslant 1$. As before, the weight can be simply determined as $w_j = a_j/(a_j + b_j)$, where this time a_j and b_j correspond to the sides of integration elements Ω_{III} and Ω_I, respectively. The discontinuous enrichment function associated with β_j is

$$\chi_j = \begin{cases} -w_j N_{j+}^{\mathrm{I}}(\boldsymbol{x}) & \text{for } \boldsymbol{x} \in \Omega_{\mathrm{I}} \\ (1 - w_j) N_{j-}^e(\boldsymbol{x}) & \text{for } \boldsymbol{x} \in \Omega_{e=\mathrm{II,III}} \end{cases}. \tag{26}$$

Appendix D presents a *Mathematica*® script that computes the weights and plots the discontinuous enrichment functions for the simple case shown in Figure 5.

Figure 6 illustrates the creation of the discontinuous enrichment functions associated with enriched DOFs $\boldsymbol{\beta}_i$ and $\boldsymbol{\beta}_j$ for a bilinear quadrilateral element. The discontinuity splits the element into integration elements $\Omega_{\mathrm{I}}, \Omega_{\mathrm{II}}$ that are connected to newly created nodes i, j. Following the procedure described above, the strong discontinuity enrichment functions χ_i and χ_j associated with these nodes are given by

$$\chi_i = \begin{cases} -w_i N_{i-}^{\mathrm{I}}(\boldsymbol{x}) & \text{for } \boldsymbol{x} \in \Omega_{\mathrm{I}} \\ (1 - w_i) N_{i+}^{\mathrm{II}}(\boldsymbol{x}) & \text{for } \boldsymbol{x} \in \Omega_{\mathrm{II}} \end{cases}, \qquad \chi_j = \begin{cases} -w_j N_{j-}^{\mathrm{I}}(\boldsymbol{x}) & \text{for } \boldsymbol{x} \in \Omega_{\mathrm{I}} \\ (1 - w_j) N_{i+}^{\mathrm{II}}(\boldsymbol{x}) & \text{for } \boldsymbol{x} \in \Omega_{\mathrm{II}} \end{cases}, \tag{27}$$

where the weights w_i and w_j are simply determined by finding the distance to the discontinuity relative to the corresponding edge length, *i.e.*, $w_i = a_i/(a_i + b_i)$ and $w_j = a_j/(a_j + b_j)$ (*cf.* Figure 6). Note that obtaining the weights requires consistency insofar as to which nodes are used to compute the distance to the discontinuity. In other words, only nodes lying on one side of the crack (whichever that side is) are used for the computation of the weights.

In the foregoing discussion, integration elements are also quadrilateral elements. There are cases, however, when a discontinuity traverses a quadrilateral element in such a way that at least one triangular integration element is needed. It is then important to note that quadrilateral elements can also be split in triangular integration elements as long as the resulting enrichment functions are able to recover the bilinear behavior of the parent element, *i.e.*, the *xy* term. This can be easily accomplished by using six-node quadratic triangles as integration elements. In either case, the resulting enrichment functions in DE-FEM ramp to zero at nodes of the original mesh, and thus, they retain local support by construction.

Figure 7 shows the creation of integration elements when dealing with a crack tip j. In this situation, the crack tip is endowed with just a weak discontinuity enrichment $\boldsymbol{\alpha}_j$ because, by definition, there is no jump in the displacement at a crack tip. Retaining the full approximation, with strong and weak enrichment, would require to prescribe $\boldsymbol{\beta}_j = \boldsymbol{0}$. This and other computer implementation details are discussed in Appendix A.
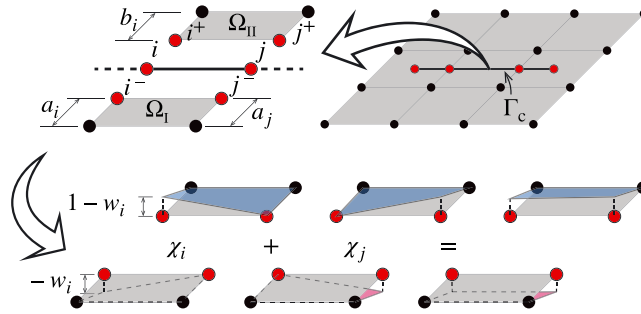

FIGURE 6 Construction of DE-FEM discontinuous enrichment functions for nodes i and j created at the intersection of a crack Γ_c with the edges of a quadrilateral element.
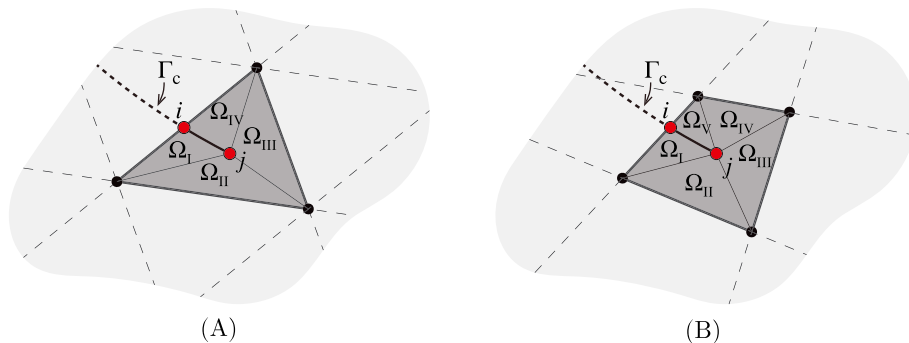

(A) (B)

FIGURE 7 Creation of integration elements for (A) triangular and (B) quadrangular elements when the crack tip ends within an element.

Following standard procedures, the local system $k_i u_i = f_i$ for the ith element is expressed as

$$\underbrace{\begin{bmatrix} k_{uu} & k_{u\alpha} & k_{u\beta} \\ k_{\alpha u} & k_{\alpha\alpha} & k_{\alpha\beta} \\ k_{\beta u} & k_{\beta\alpha} & k_{\beta\beta} \end{bmatrix}}_{k_i} \underbrace{\begin{bmatrix} U \\ \alpha \\ \beta \end{bmatrix}}_{u_i} = \underbrace{\begin{bmatrix} f_u \\ f_\alpha \\ f_\beta \end{bmatrix}}_{f_i}, \tag{28}$$

where the subscript u refers to the standard part of the approximation, subscripts α and β indicate the weak and strong enriched contributions, respectively, and

$$k_{uu} = \int_{\Omega_i} B_u^\mathsf{T} D B_u \ \mathrm{d}\Omega, \tag{29a}$$

$$k_{\alpha u} = \int_{\Omega_i} B_\alpha^\mathsf{T} D B_u \ \mathrm{d}\Omega = k_{u\alpha}^\mathsf{T}, \tag{29f}$$

$$k_{\alpha\alpha} = \int_{\Omega_i} B_\alpha^\mathsf{T} D B_\alpha \ \mathrm{d}\Omega, \tag{29b}$$

$$k_{\beta u} = \int_{\Omega_i} B_\beta^\mathsf{T} D B_u \ \mathrm{d}\Omega = k_{u\beta}^\mathsf{T}, \tag{29g}$$

$$k_{\beta\beta} = \int_{\Omega_i} B_\beta^\mathsf{T} D B_\beta \ \mathrm{d}\Omega, \tag{29c}$$

$$k_{\alpha\beta} = \int_{\Omega_i} B_\alpha^\mathsf{T} D B_\beta \ \mathrm{d}\Omega = k_{\beta\alpha}^\mathsf{T}, \tag{29h}$$

$$f_u = \int_{\Omega_i} N_u^\mathsf{T} b \ \mathrm{d}\Omega + \int_{\partial\Omega_i} N_u^\mathsf{T} \bar{t} \ \mathrm{d}\Gamma, \tag{29d}$$

$$f_\beta = \int_{\Omega_i} N_\beta^\mathsf{T} b \ \mathrm{d}\Omega + \int_{\partial\Omega_i} N_\beta^\mathsf{T} \bar{t} \ \mathrm{d}\Gamma. \tag{29i}$$

$$f_\alpha = \int_{\Omega_i} N_\alpha^\mathsf{T} b \ \mathrm{d}\Omega + \int_{\partial\Omega_i} N_\alpha^\mathsf{T} \bar{t} \ \mathrm{d}\Gamma, \tag{29e}$$

In addition, D represents the material constitutive matrix, here assumed linear elastic. Because of the form of the enrichment functions in DE-FEM, these integrals are evaluated numerically through Gauss quadrature on the interior of integration elements where the functions involved are well behaved. The global stiffness matrix and force vector are obtained by considering the contribution of all elements in the discretization. In other words, denoting with $\mathbb{A}$ the finite element assembly operator, $K = \mathbb{A}_i \, k_i$ and $F = \mathbb{A}_i \, f_i$.

2.3 | Cohesive formulation

When an element is crossed by a strong discontinuity, a corresponding cohesive element is defined with the purpose of simplifying the generation of its stiffness matrix contribution and assembly procedures. In the rest of the paper, we therefore use the term *elements* to identify those used to discretize the continuum and *cohesive elements* for those that identify the portion of the discontinuity defined by the intersection of an element and the discontinuity itself. Clearly, a cohesive discontinuity is defined as the union of all its cohesive elements.

In the discretized form of Equation (19), the cohesive traction contribution

$$\Pi_\mathrm{c} \equiv \int_{\Gamma_\mathrm{c}} [\![v]\!] \cdot t_\mathrm{c} \ \mathrm{d}\Gamma \tag{30}$$

is obtained by the individual contribution of the cohesive elements, *i.e.*, $\Pi_\mathrm{c} = \sum_e \Pi_\mathrm{c}^e$. In the following, all quantities are assumed at the element level, and thus, we omit the superscript e. Figure 8 shows element Ω_i crossed by a cohesive crack. The position along the discontinuity segment, defined by points i and j, is described by means of a master coordinate ξ following the traditional isoparametric formulation, *i.e.*, $x = x(\xi), -1 \leqslant \xi \leqslant 1$. The displacement jump at the discontinuity is expressed as $\delta \equiv [\![u]\!] = u^+ - u^-$ with $u^\pm \equiv u^h|_{\Gamma_\mathrm{c}^\pm}$. The jump along the discontinuity is interpolated by using standard hat shape functions and the values of the strong enriched DOFs as

$$\delta(\xi) = \underbrace{(N \otimes I)}_{M} \begin{bmatrix} \beta_i \\ \beta_j \end{bmatrix}, \tag{31}$$

where $N = \begin{bmatrix} \frac{1-\xi}{2} & \frac{1+\xi}{2} \end{bmatrix}$, I is the $d \times d$ identity matrix, and $\otimes$ denotes the Kronecker product. Noteworthy, the displacement jump at the discontinuity is determined by considering quantities that are local to the discontinuity: the hat shape functions and the enriched DOFs. This fact has major consequences in the implementation of the cohesive formulation. Indeed, the evaluation
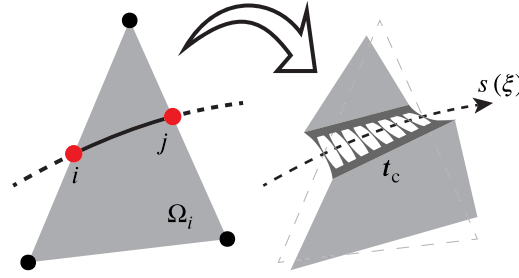
FIGURE 8 Schematic of a cohesive crack crossing a finite element Ω_i. The figure shows the discontinuity coordinate s, parameterized by a parent coordinate ξ $(-1 \leqslant \xi \leqslant 1)$, and the cohesive traction t_c.

of the cohesive element contributions can be done by only integrating along the line elements that define the discontinuity, as shown by the cohesive contributions k_c to the tangent stiffness matrix $k_{\beta\beta}$ and f_c to the force vector f_β:

$$k_c = \int_{\Gamma_c} M^\intercal \frac{\partial t_c}{\partial \delta} M \, d\Gamma \quad \text{and} \quad f_c = \int_{\Gamma_c} M^\intercal t_c \, d\Gamma, \tag{32}$$

where t_c is the vector of cohesive tractions that depends on the cohesive law. As before, the contribution of all cohesive elements is assembled as $\mathbb{A}_i \, k_{c,i}$ and $\mathbb{A}_i f_{c,i}$ for the global stiffness matrix and force vector, respectively. Noteworthy, the computer implementation is the same as that of traction-free cracks, the difference only being in the creation of cohesive elements when cohesive cracks are present.

2.4 | Comparison between DE-FEM and X/GFEM

Important differences between X/GFEM and DE-FEM are listed below.

(i) In DE-FEM, all standard nodes conserve the Kronecker property (the associated DOFs represent the displacement at that location); indeed, since enrichment functions of DE-FEM vanish at nodes of the original mesh, DOFs associated with these nodes retain their physical interpretation. In X/GFEM, however, unless special enrichment functions are used—*e.g.*, by using *shifting* in the case of polynomial enrichments—the Kronecker property is lost in mesh nodes that are enriched.

(ii) In DE-FEM, enrichments are nonzero only in elements cut by the discontinuities (enrichment functions are local by construction). On the contrary, enrichments in X/GFEM are localized by a multiplication with the standard shape functions. This has been a major issue in the X/GFEM community because enrichments may introduce parasitic terms into the formulation and degrade the solution accuracy.[19]

(iii) Enriched DOFs are associated with new nodes created along the discontinuities and directly represent the crack opening in the case of strong enriched DOFs. In X/GFEM, on the contrary, the enriched DOFs are attached to nodes of the original mesh and represent the crack opening only after interpolation.

(iv) Most importantly, imposing essential (Dirichlet) boundary conditions in DE-FEM is as straightforward as in standard FEM. Conversely, X/GFEM needs special formulations to accomplish this when enrichment functions do not vanish at non-homogeneous Dirichlet boundaries (*e.g.*, by using the penalty method or Lagrange multipliers[17]); this increases the complexity of implementing X/GFEM in standard FEM packages.

(v) It was shown that the cohesive contributions to the stiffness matrix and the force vector only depend on enriched DOFs β and shape functions defined along cohesive elements. Contrary to this, the cohesive contributions in X/GFEM are generated at the element level since the displacement jump is obtained after interpolating the displacement field at both sides of the discontinuity.

(vi) Regarding the computer implementation, DE-FEM is considerably simpler to program compared to X/GFEM. Perhaps the most important difference lies in implementing essential boundary conditions, as no major modification to a standard FEM package is needed with DE-FEM. In addition, since enriched DOFs are tied to new enriched nodes created along a discontinuity and not to nodes of the original discretization, there is no need for additional array data structures to accommodate for enriched DOFs in standard mesh nodes (as it may be the case in X/GFEM implementations[20]). Cohesive contributions in DE-FEM are obtained by only integrating over cohesive elements, whereas in X/GFEM such contributions are obtained only by processing the bulk element. Finally, an immediate consequence of mesh nodes keeping their Kronecker property is that less post-processing is required in DE-FEM. Implementation details of DE-FEM in standard FEM packages are thoroughly discussed in Appendix A.
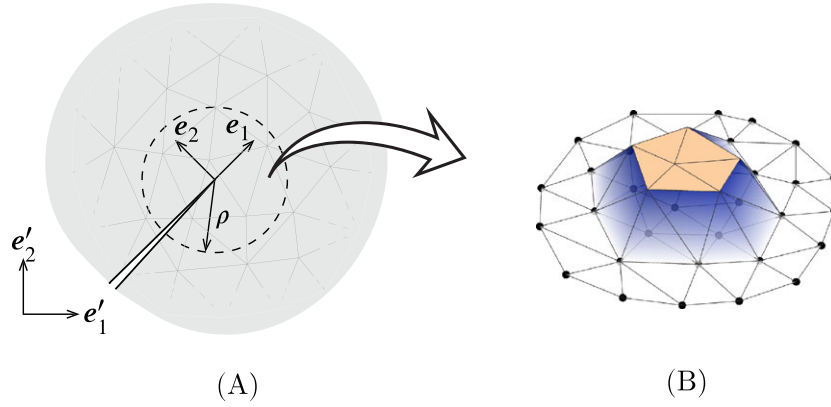
FIGURE 9 (A) Crack tip and conventions for the computation of the domain integral in Equation (34): The domain integral is computed on elements that intersect a circle of radius ρ using the weight function q_1 depicted in (B).

2.5 | Stress intensity factors

In some of the examples found later in this manuscript, DE-FEM is used to extract stress intensity factors (SIFs). Mixed-mode SIFs are obtained following the formulation by Yau *et al.*[21]:

$$M^{(1,2)} = 2c\left(K_{\mathrm{I}}^{(1)}K_{\mathrm{I}}^{(2)} + K_{\mathrm{II}}^{(1)}K_{\mathrm{II}}^{(2)}\right) \text{ with } c = \begin{cases} \frac{1-\nu^2}{E} & \text{for plane strain} \\ \frac{1}{E} & \text{for plane stress} \end{cases}, \tag{33}$$

where $K_{\mathrm{I}}, K_{\mathrm{II}}$ denote SIFs for modes I and II, respectively, the superscripts refer to two independent equilibrium states, and $M^{(1,2)}$ denotes the conservation integral considering their superposition. In this work, we use the domain representation of such integral[22]:

$$M^{(1,2)} = \int_A \left[\left(-\sigma_{ik}^{(1)}\varepsilon_{ik}^{(2)}\delta_{1j} + \sigma_{ij}^{(1)}\frac{\partial u_i^{(2)}}{\partial x_1} + \sigma_{ij}^{(2)}\frac{\partial u_i^{(1)}}{\partial x_1}\right)\frac{\partial q_1}{\partial x_j}\right] \mathrm{d}A, \tag{34}$$

where the terms are taken with respect to a coordinate system that is local to the crack tip (see Figure 9A). The weight function q_1 has unit magnitude in finite elements completely enclosed by the circle of radius ρ, ramping down to zero at nodes of intersected elements (see Figure 9B). Note that elements fully enclosed by the circle do not contribute to the interaction integral since $\partial q_1/\partial x_j = 0$.

By choosing an appropriate equilibrium state, it is possible to obtain the mixed-mode SIFs from Equations (33) and (34). If, for example, we assume an auxiliary equilibrium state of pure mode I, then $K_{\mathrm{I}}^{(2)} = 1, K_{\mathrm{II}}^{(2)} = 0$ and Equation (33) yields the mode I SIF for the current state as $K_{\mathrm{I}}^{(1)} = M^{(1,2)}/(2c)$, where the domain integral is evaluated with $\boldsymbol{u}^{(2)} = \boldsymbol{u}_{K_{\mathrm{I}}}$ and $\boldsymbol{\sigma}^{(2)} = \boldsymbol{\sigma}_{K_{\mathrm{I}}}$ (Equations (C1a) and (C3a)), respectively, in Appendix C). Similarly, by taking a pure mode II as the auxiliary field, $K_{\mathrm{I}}^{(2)} = 0, K_{\mathrm{II}}^{(2)} = 1$, and $K_{\mathrm{II}}^{(1)} = M^{(1,2)}/(2c)$.

3 | NUMERICAL EXAMPLES

Unless otherwise specified, in the following examples we use plane strain conditions and consistent units when these are not specified. Both weak and strong enrichment functions as specified by Equation (20) are used throughout to ensure independent linear fields at each side of the discontinuities. In addition, a quadrature rule that exactly integrates integration elements is also used. In the X/GFEM examples the two sub-elements generated when an element is cut by a discontinuity are triangulated, and in each triangular domain we used a three-point Gauss quadrature scheme.

3.1 | A discontinuous patch test

This example shows the capability of the new formulation to generate two kinematically independent configurations when a domain is arbitrarily cut by a discontinuity. This will be demonstrated by means of a patch test. It bears emphasis that due to the simplicity in the application of essential boundary conditions in DE-FEM, the discontinuous patch test given here is simpler than that proposed for the X/GFEM by Dolbow and Devan.[23]
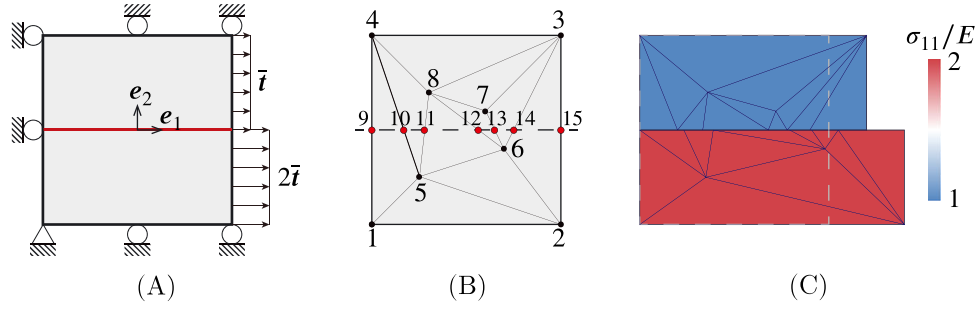
FIGURE 10 (A) Schematic for the discontinuous patch test; (B) a possible discretization of the problem using triangular elements; and (C) deformed configuration and stress distribution.

Consider the square plate shown in Figure 10A with side $L = 1$. The plate is cut into two parts by a crack at $x_2 = 0$ (solid red line), and tractions $\bar{t} = t\, e_1$ and $2\bar{t}$ are applied to the right edge above (Γ_t^+) and below (Γ_t^-) the crack, respectively. A possible discretization of the problem is given in Figure 10B, where new nodes ($\bullet$) have been placed along the crack at the intersection with the element edges. It is worth noting that since both weak and strong discontinuity enrichments are considered, each of these nodes is associated with four DOFs (two for α_i and two for β_i).

Given that the force is acting in the x_1 direction, the force vector acting on nodes 2, 3, and 15 can be readily obtained by performing the following 1-D integration

$$f = \int_{\Gamma_t^+} N^\mathsf{T} t \; \mathrm{d}\Gamma + \int_{\Gamma_t^-} 2N^\mathsf{T} t \; \mathrm{d}\Gamma = \begin{bmatrix} \frac{7t}{8} & \frac{5t}{8} & \frac{3t}{4} & -\frac{t}{8} \end{bmatrix}^\mathsf{T}, \tag{35}$$

where $N = \begin{bmatrix} N_2 & N_3 & \psi_{15} & \chi_{15} \end{bmatrix}$, and ψ_{15} has a unit value at node 15 and ramps linearly to zero at nodes 2 and 3 (no scaling is used here for the weak enrichment). Finally, it is worth noting that a node is also created along the constrained left edge of the plate. Because there is no displacement jump at x_9, $\beta_9 = 0$ and α_9 can be readily obtained from Equation (20) as

$$\alpha_9 = u^h(x_9) - N_1(x_9) U_1 - N_2(x_4) U_4 = 0. \tag{36}$$

Prescribing α_9 and β_9 is as straightforward as in the standard FEM.

The resulting deformed configuration, together with the stress field, is reported in Figure 10C. It can be seen that the formulation passes this discontinuous patch test, *i.e.*, both parts at either side of the crack have their independent constant stress field. It bears emphasis that, as expected, a zero value was computed for all enriched DOFs concerning the behavior in the x_2 direction. Unneeded enrichments are therefore not active.

Once again, we would like to stress the importance of using both weak and strong enrichment functions. In view of reducing computational requirements, one may be tempted to use only the strong discontinuity enrichment which, after all, is responsible for representing the jump in the displacement field. However, this approach would fail the discontinuous patch test because there are insufficient DOFs to represent independent linear fields at each side of the strong discontinuity.

3.2 | DE-FEM convergence properties

In this example, we demonstrate the convergence properties of DE-FEM for classical 2-D plane strain mode I and mode II problems. Consider a square plate with length $L = 2$ discretized using a structured mesh of three-node triangles. A horizontal crack is defined from the left edge to the center of the plate. The displacement at the plate boundary is prescribed by using the crack-tip displacement fields $\bar{u}$ for modes I and II, as given in Appendix C in Equation (C1a) with $K_\mathrm{I} = 1$ and Equation (C1b) with $K_\mathrm{II} = 1$, respectively. The boundary condition $u = \bar{u}$ is applied not only at all mesh nodes along the plate boundary but also to the discontinuity node created at the intersection between the plate boundary and the crack (at $x = -e_1$).

Figure 11 shows the deformed configurations for both mode I and mode II obtained by the standard FEM and by DE-FEM. For the latter, the displacement field is accurately represented only after post-processing the displacement field in elements traversed by the crack.

The convergence behavior is now characterized by measuring the error in the energy norm, defined as

$$\frac{\|u - u^h\|_{E(\Omega)}}{\|u\|_{E(\Omega)}} = \frac{\sqrt{\int_\Omega (\varepsilon - \varepsilon^h)^\mathsf{T} D (\varepsilon - \varepsilon^h) \, \mathrm{d}\Omega}}{\sqrt{\int_\Omega \varepsilon^\mathsf{T} D\varepsilon \, \mathrm{d}\Omega}}. \tag{37}$$
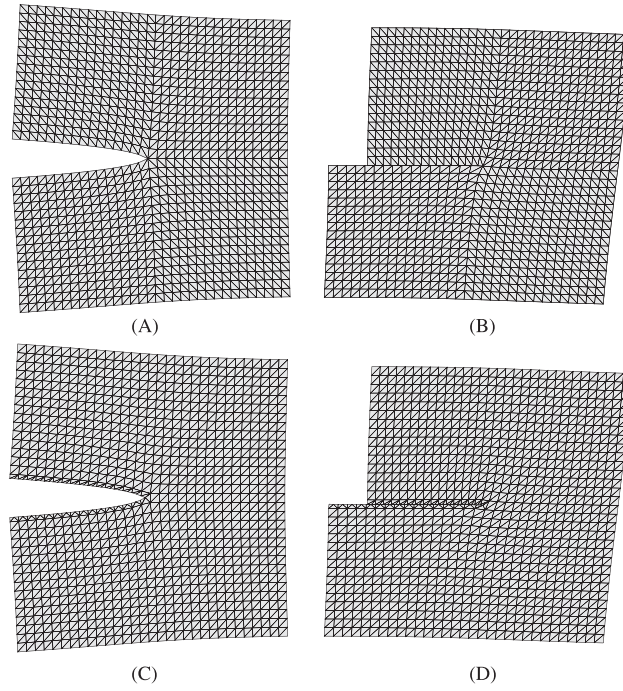
FIGURE 11 Modes I and II deformed configurations for (A, B) standard FEM and (C, D) DE-FEM. The latter are obtained after post-processing.
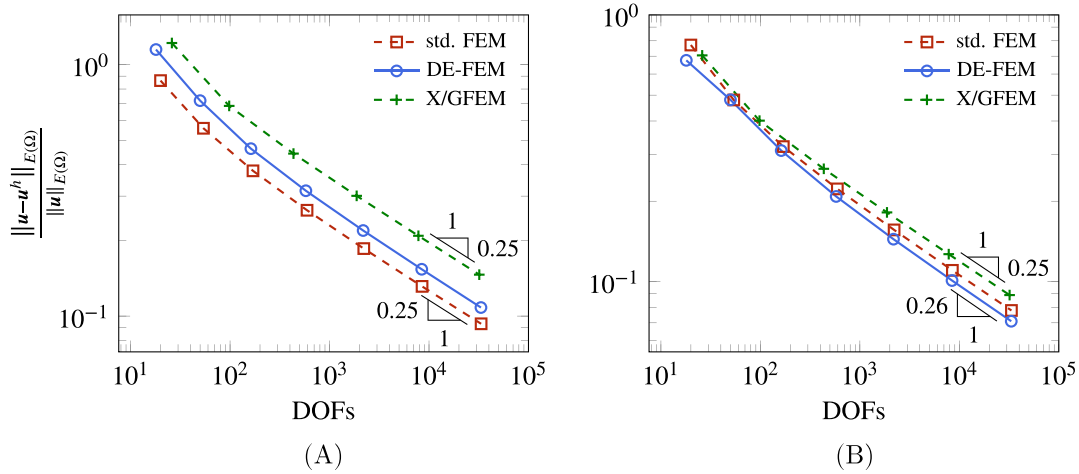

FIGURE 12 Convergence results for the error in the energy norm for (A) mode I and (B) mode II problems.

Figure 12 shows this error as a function of the number of DOFs for modes I (A) and II (B). These figures show that DE-FEM converges at the same rate as that of the standard FEM with the use of matching meshes and X/GFEM with step enrichment alone. In the case of mode II, DE-FEM is even more accurate than standard FEM, and it is more accurate than X/GFEM with step enrichment in both cases.

As mentioned in the previous example, the formulation does not pass the patch test if only the strong discontinuity enrichment is used. In terms of convergence, using the strong enrichment alone results in convergence rates of 0.21 and 0.22 for modes I and II, respectively.

3.3 | Square plate with double-edge cracks

This example aims at recovering the mode I SIF for a plate containing two edge cracks for different values of the ratio a/W (*cf.* Figure 13A). Irwin[24] reported that an approximation of the SIF for this problem can be expressed as $K_\mathrm{I} = K_0 \phi_a$, where

$$K_0 = \sigma \sqrt{\pi a}, \qquad \phi_a = \sqrt{\frac{2W}{\pi a} \tan\left(\frac{\pi a}{2W}\right)}. \tag{38}$$
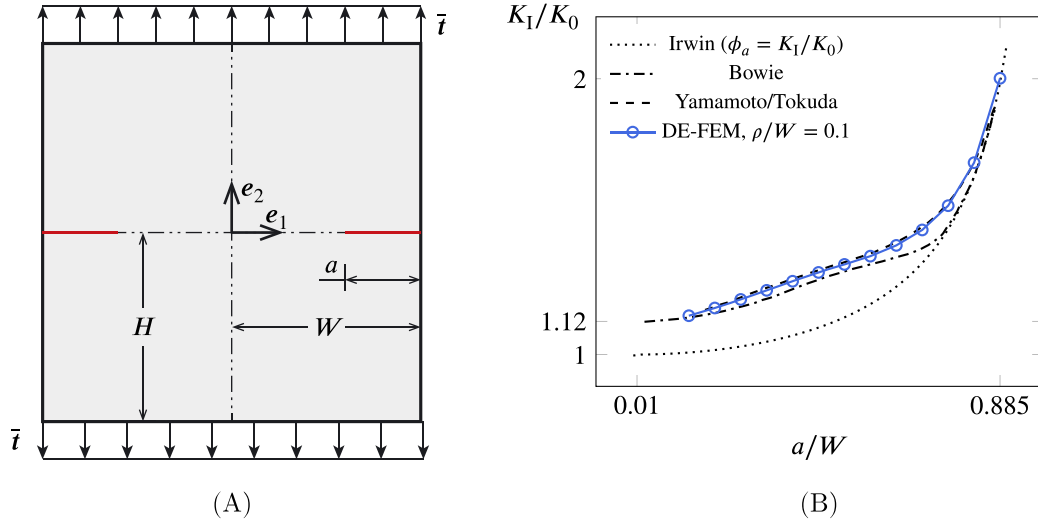
FIGURE 13 (A) Square plate with double-edge cracks; (B) normalized mode I stress intensity factor as a function of the crack length to semi-width ratio a/W.

This problem was then solved analytically by Bowie[25] using a conformable mapping technique for $H/W = \{1, 3\}$. Yamamoto and Tokuda[26] later solved the problem for $H/W = \{1, 2.75\}$ by mixing an analytical function with results from finite element analysis. They showed that their results are more accurate than Bowie's, with an error of about 0.5%.

The DE-FEM results for $H/W = 1$ are reported in Figure 13B and were obtained by using an unstructured mesh of constant-strain triangles discretizing half of the domain because of symmetry. A non-uniform mesh size was used in the discretization, varying from $h/W = 0.2$ at $x_2 = \pm H$ to $h/W = 0.002$ at $x_2 = 0$. The use of this fine mesh is needed because results are compared with the accurate technique of Yamamoto and Tokuda mentioned above, and the proposed enrichment functions do not capture the stress singularity at the crack tip. For the computation of the mode I SIF, a radius $\rho/W = 0.1$ was used. The figure shows that DE-FEM is able to achieve a more accurate result than that of Bowie, but not as accurate as that of Yamamoto and Tokuda. Nevertheless, considering the fact that the latter mixes analytic and numerical results, and that DE-FEM does not make use of any singularity enrichment, the accuracy of the prediction is remarkable.

3.4 | Square plate with centered slanted crack

In this example, we study the extraction of SIFs in mixed-mode loading. Consider a square plate of side $2W = 10$ subjected to a traction $\pm \bar{t} e_2$ at $x_2 = \pm W$ as shown in Figure 14. A crack of length $2a = 1$ is situated at the center of the plate and inclined at an angle φ. The SIFs for this problem are given by[27]

$$K_{\mathrm{I}} = \bar{t}\sqrt{\pi a}\cos^2(\varphi) \quad \text{and} \quad K_{\mathrm{II}} = \bar{t}\sqrt{\pi a}\sin(\varphi)\cos(\varphi). \tag{39}$$
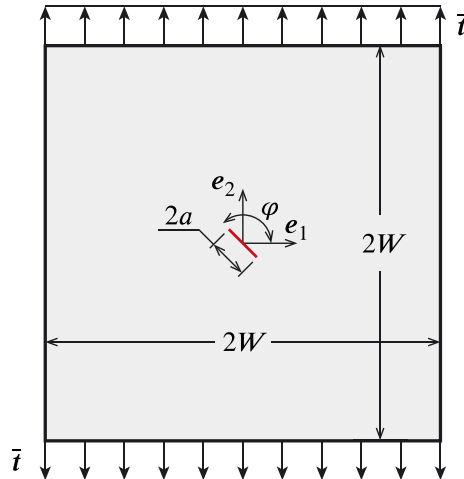

FIGURE 14 Square plate with centered crack slanted at an angle φ from the horizontal line.
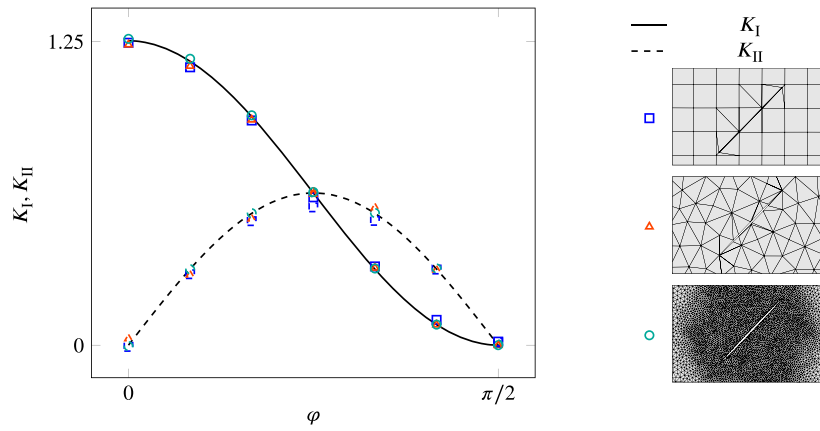
FIGURE 15 Stress intensity factors K_I and K_{II} computed with $\rho/W = 0.1$ by placing a crack at different angles. The legends show deformed configurations for $\varphi = \pi/4$ for coarse structured and unstructured meshes (with mesh size $h/W = 0.05$) and for a fine unstructured mesh.

Results for this problem are given in Figure 15, where the legends show the type of mesh used and the deformed configuration for $\varphi = \pi/4$. It can be seen that even coarse meshes give accurate values of the mixed-mode SIFs. The results for a fine unstructured finite element mesh lie on top of the theoretical values.

3.5 | Beam with perfectly bonded cohesive interface

This example illustrates the use of DE-FEM with a cohesive crack. Consider a notched beam of length $L = 450$ mm, height $h = 100$ mm, and thickness $b = 100$ mm, with a notch $a = 20$ mm as illustrated in Figure 16A. The beam is composed by an elastic material with Young's modulus $E = 2 \times 10^4$ N/mm^2 and Poisson's ratio $\nu = 0.2$. Boundary conditions include a roller
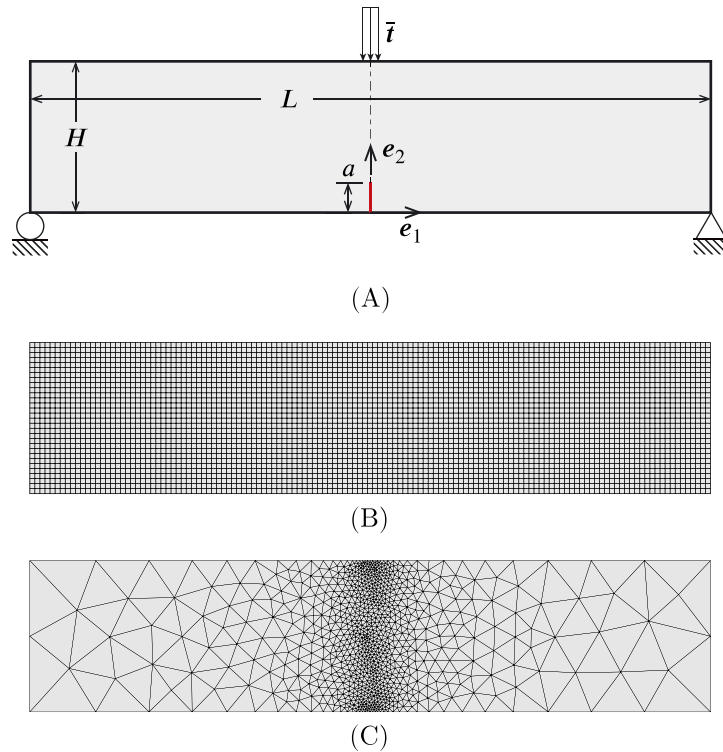

FIGURE 16 (A) Schematic of the bending beam with a cohesive discontinuity passing through the center line; discretizations used include meshes of (B) Q4 and (C) T3 elements.
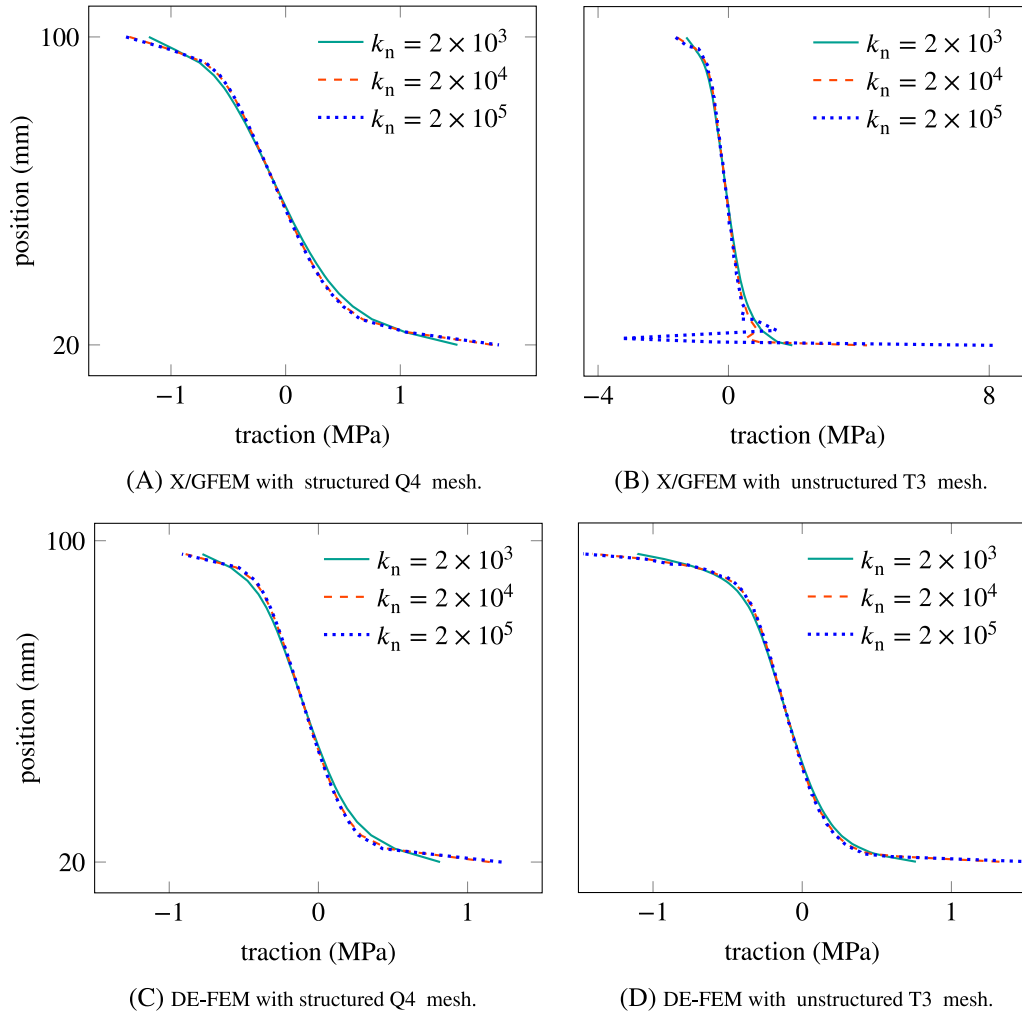
FIGURE 17 Comparison between X/GFEM (top) with DE-FEM (bottom) showing the traction profile at the centerline of the beam of Figure 16. Normal stiffness k_n in N/mm^3.

support at its lower-left corner, a fixed support at its lower-right corner, and an applied traction $\bar{t} = -1 \text{ kN/mm}^2 e_2$. The beam is crossed by a discontinuity passing through the center line. A traction-free discontinuity represents the notch, while the rest of the discontinuity line is assigned increasing values of the normal stiffness, *i.e.*, $k_n = \left\{2 \times 10^3, 2 \times 10^4, 2 \times 10^5\right\}$ N/mm^3, to simulate perfect material bonding. Rigid-body rotation is prevented by taking a tangential stiffness $k_t = 1$ N/mm^3. This problem was first studied by Rots[28] using interface elements and later by Simone[16] in the context of X/GFEM. Simone showed that, unless a structured finite element mesh is used, the cohesive tractions at the interface suffer from high oscillations close to the notch as the normal stiffness coefficient k_n increases.

A structured mesh of bilinear quadrangles and an unstructured mesh of linear triangles, as shown in Figure 16B,C, are employed. Cohesive elements are integrated using a two-point Gauss-Lobatto rule. The results for this study are given in Figure 17, where the cohesive traction profile (in abscissas) is plotted against its position along the beam centerline (ordinates). As it was reported in the study of Simone,[16] the traction profile resulting from the X/GFEM simulation is smooth when dealing with a structured mesh of quadrangles (Figure 17A), but the use of an unstructured triangular mesh produces oscillations in the cohesive traction profile as k_n is increased (Figure 17B). The same discretizations are used with DE-FEM, and while the structured quadrangular mesh gives roughly the same result as X/GFEM (Figure 17C), it can be seen that the traction profile for the unstructured triangular mesh shows no oscillations (Figure 17D).

4 | CONCLUDING REMARKS

In this article, we have introduced DE-FEM, a novel enriched finite element formulation for the solution of problems with both weak and strong discontinuities. While emphasis has been placed on the solution of problems in fracture mechanics,

the formulation is general and can therefore be applied to solve other partial differential equations where the field is C^{-1}– and/or C^0–continuous. When modeling strong discontinuities, both weak and strong enrichment functions are used. We showed that the new formulation converges at the same rate as the standard FEM with meshes that conform to the discontinuities. Furthermore, we showed that DE-FEM can be used to extract SIFs with an accuracy commensurate with the fact that the proposed enrichment functions do not capture the stress singularity at the crack tip.

By design, DE-FEM inherits the approximation properties of IGFEM because of the construction of the finite-dimensional approximation space (see Equation (20)). DE-FEM can therefore seamlessly model weak and strong discontinuities, a desirable feature when a crack develops at the interface between two different materials. Apart from the improved kinematics, a notable feature of DE-FEM is the placement of nodes with enriched DOFs along a discontinuity. This clearly gives DE-FEM an edge over X/GFEM, as the complexity of the latter in terms of computer implementation has hindered its wide adoption in commercial software packages.[29] In fact, implementing DE-FEM in a standard finite element package requires mainly a means to partition elements into integration elements—with their corresponding routine for computing local arrays—and a post-processing engine for visualizing results. Everything else, from the mesh data structures to the enforcement of essential boundary conditions, remains roughly the same.

The most striking advantage of DE-FEM is the enforcement of essential boundary conditions. This was demonstrated in an earlier publication,[14] where the IGFEM formulation (weak enrichments only) coupled to Lagrange multipliers solved the fundamental issue of artificial oscillations in the traction field while imposing Dirichlet boundary conditions on an external boundary that does not match the mesh. Here, we have demonstrated that the same feature holds when constraining enriched DOFs along a line internal to the computational domain using penalty augmentation. It bears emphasis that constraining extra DOFs within the domain in X/GFEM using the simple penalty augmentation approach yields unreliable results.[16] This is clearly a shortcoming of the classical X/GFEM formulation. Even though headway has been made for imposing Dirichlet boundary conditions on non-matching meshes,[15,30] the procedures are far from being trivial.

ORCID

Alejandro M. Aragón http://orcid.org/0000-0003-2275-6207
Angelo Simone http://orcid.org/0000-0001-9726-0068

REFERENCES

1. Duarte CA, Hamzeh ON, Liszka TJ, Tworzydlo WW. A generalized finite element method for the simulation of three-dimensional dynamic crack propagation. *Comput Methods App Mech Eng*. 2001;190:2227-2262.

2. Moës N, Dolbow J, Belytschko T. A finite element method for crack growth without remeshing. *Int J Numer Methods Eng*. 1999;46(1):131-150.

3. Mayer UM, Popp A, Gerstenberger A, Wall WA. 3D fluid–structure-contact interaction based on a combined XFEM FSI and dual mortar contact approach. *Computat Mech*. 2010;46(1):53-67.

4. Villanueva CH, Maute K. Density and level set-XFEM schemes for topology optimization of 3-D structures. *Computat Mech*. 2014;54(1):133-150.

5. Chessa J, Smolinski P, Belytschko T. The extended finite element method (XFEM) for solidification problems. *Int J Numer Methods Eng*. 2002;53(8):1959-1977.

6. Babuška I, Banerjee U. Stable generalized finite element method (SGFEM). *Comput Methods Appl Mech Eng*. 2012;201–204:91-111.

7. Gupta V, Duarte CA, Babuška I, Banerjee U. A stable and optimally convergent generalized FEM (SGFEM) for linear elastic fracture mechanics. *Comput Methods Appl Mech Eng*. 2013;266:23-39.

8. Soghrati S, Aragón AM, Duarte CA, Geubelle PH. An interface-enriched generalized FEM for problems with discontinuous gradient fields. *Int J Numer Methods Eng*. 2012;89(8):991-1008.

9. Soghrati S. Hierarchical interface-enriched finite element method: an automated technique for mesh-independent simulations. *J Computat Phys*. 2014;275:41-52.

10. Soghrati S, Duarte CA, Geubelle PH. An adaptive interface-enriched generalized FEM for the treatment of problems with curved interfaces. *Int J Numer Methods Eng*. 2015;102(6):1352-1370.

11. Aragón AM, Soghrati S, Geubelle PH. Effect of in-plane deformation on the cohesive failure of heterogeneous adhesives. *J Mech Phys Solids*. 2013;61(7):1600-1611.

12. Soghrati S, Geubelle PH. A 3D interface-enriched generalized finite element method for weakly discontinuous problems with complex internal geometries. *Comput Methods Appl Mech Eng*. 2012;217–220:46-57.

13. Soghrati S, Barrera JL. On the application of higher-order elements in the hierarchical interface-enriched finite element method. *Int J Numer Methods Eng*. 2016;105(6):403-415.

14. Cuba-Ramos A, Aragón AM, Soghrati S, Geubelle PH, Molinari J-F. A new formulation for imposing Dirichlet boundary conditions on non-matching meshes. *Int J Numer Methods Eng*. 2015;103(6):430-444.

15. Moës N, Béchet E, Tourbier M. Imposing Dirichlet boundary conditions in the extended finite element method. *Int J Numer Methods Eng*. 2006;67(12):1641-1669.

16. Simone A. Partition of unity-based discontinuous elements for interface phenomena: computational issues. *Commun Numer Methods Eng*. 2004;20(6):465-478.

17. Babuška I, Banerjee U, Osborn JE. Survey of meshless and generalized finite element methods: a unified approach. *Acta Numer*. 2003;12:1-125.

18. Felippa CA. Introduction to Finite Element Methods (ASEN 5007). Lecture Notes, Department of Aerospace Engineering Sciences, University of Colorado at Boulder; 2016.

19. Fries T-P. A corrected XFEM approximation without problems in blending elements. *Int J Numer Methods Eng*. 2008;75(5):503-532.

20. Sukumar N, Prévost J-H. Modeling quasi-static crack growth with the extended finite element method Part I: computer implementation. *Int J Solids Struct*. 2003;40(26):7513-7537.

21. Yau JF, Wang SS, Corten HT. A mixed-mode crack analysis of isotropic solids using conservation laws of elasticity. *J Appl Mech*. 1980;47(2):335-341.

22. Shih CF, Asaro RJ. Elastic-Plastic Analysis of Cracks on Bimaterial Interfaces: Part I—Small Scale Yielding. *J Appl Mech*. 1988;55(2):299-316.

23. Dolbow JE, Devan A. Enrichment of enhanced assumed strain approximations for representing strong discontinuities: addressing volumetric incompressibility and the discontinuous patch test. *Int J Numer Methods Eng*. 2004;59(1):47-67.

24. Irwin GR. Fracture. In: Flügge S, ed. *Elasticity and Plasticity*, Encyclopedia of Physics, vol. VIa/2. Berlin, Gottingen, Heidelberg: Spring-Verlag; 1958:551-590.

25. Bowie OL. Rectangular tensile sheet with symmetric edge cracks. *J Appl Mech*. 1964;31(2):208-212.

26. Yamamoto Y, Tokuda N. Determination of stress intensity factors in cracked plates by the finite element method. *Int J Numer Methods Eng*. 1973;6(3):427-439.

27. Anderson TL. *Fracture Mechanics: Fundamentals and Applications*. Boca Raton, FL:CRC press; 2005.

28. Rots JG. Computational Modeling of Concrete Fracture. *Ph.D. Thesis*; Delft University of Technology, Delft, the Netherlands; 1988.

29. Kreissl S, Maute K. Levelset based fluid topology optimization using the extended finite element method. *Struct Multi Optimi*. 2012;46(3):311-326.

30. Dolbow J, Harari I. An efficient finite element method for embedded interface problems. *Int J Numer Methods Eng*. 2009;78(2):229-252.

31. Aragón AM, Molinari J-F. A hierarchical detection framework for computational contact mechanics. *Comput Methods Appl Mech Eng*. 2014;268:574-588.

32. Simone A, Wells GN, Sluys LJ. From continuous to discontinuous failure in a gradient-enhanced continuum damage model. *Comput Methods Appl Mech Eng*. 2003;192(41–42):4581-4607.

APPENDIX A: COMPUTER IMPLEMENTATION

Next, the implementation of DE-FEM in a general purpose finite element code is detailed with the aid of pseudo-code and an informal description. The computer implementation of DE-FEM can be roughly subdivided in the tasks described below.

Mesh-discontinuity interaction The mesh independence of DE-FEM does not come for free. The complexity of the creation of a matching mesh in standard FEM is transferred to the mesh-discontinuity interaction and the corresponding enriched formulation. A robust geometric engine is needed for the modifications to the mesh data structure when discontinuities are present in the computational domain. The pseudo-code for the mesh-discontinuity interaction procedure is listed in Algorithm 1.

The geometric engine first detects the finite elements that are crossed by the discontinuities. Once an element has been tagged, new nodes are created at the element edge-discontinuity intersections. An approach appealing for computer implementation when dealing with strong discontinuities is to create double nodes, one for two weak DOFs and one for two strong DOFs; this simplifies the post-processing step for visualization as each node is correctly connected to integration elements at either side of a crack. If an element is only partially crossed by a crack, only one node is created within the element domain to hold the weak DOFs; since there is no displacement jump at the tip, there is no need to add a node for strong DOFs.

Noteworthy, the same data structures used in standard FEM can be used with DE-FEM with no modification for storing information related to enriched nodes; new nodes are added to the original node array, and enriched DOFs are stored in

the same solution vector as standard DOFs. Assuming zero-indexed arrays, any DOF can be accessed in constant time from the solution vector by multiplying the node id (either standard or enriched) by the number of DOFs per node and adding the desired DOF.

Algorithm 1 Mesh-discontinuity interaction

Input: A mesh $\mathcal{M} := \left\{ \mathcal{N}, \mathcal{E} \right\}$ (node and element sets) and a discontinuity set $\mathcal{D}$

    function INTERACT($\mathcal{M}, \mathcal{D}$)

        for $e_i \in \mathcal{E}$ **do**   *– for each element*

            for $d_i \in \mathcal{D}$ **do**   *– for each discontinuity*

                $\mathcal{I} \leftarrow e_i \cap d_i$ *– find intersection*

                if $\mathcal{I} \neq \emptyset$ **then**

                    $\mathcal{E} \leftarrow \mathcal{E} \cup \mathrm{subdivide}(\mathcal{I}, e_i)$ *– create integration elements*

                    if $\mathrm{isCohesive}(d_i)$ **then**

                        $\mathcal{E} \leftarrow \mathcal{E} \cup \mathrm{cohesive}(\mathcal{I}, d_i)$ *– add cohesive element*

                    for $n_k \in \mathcal{I}$ **do**   *– for each new node*

                      $\mathcal{N} \leftarrow \mathcal{N} \bigcup \left\{ n_k, n_k \right\}$ *– add duplicates to the mesh*

                      $w_k \equiv \left\{ w_\psi, w_\chi \right\} \leftarrow \mathrm{weights}\,(k)$ *– store enrichment weights*

        return $w, \mathcal{N}, \mathcal{E}$

Nodes are connected by cohesive elements if the problem deals with cohesive cracks. In addition, the element sub-domains at both sides of the discontinuity are divided into integration elements that will later be used in the integration and assembly procedures. Elements that are partially crossed are also subdivided into integration elements that are created with the inner tip node as one of the vertices. All of this implies that *(i)* the parent element is no longer used in the assembly process and *(ii)* the mesh data structure has to be modified accordingly to include the new nodes and integration elements.

The geometric engine is also responsible for storing the weights for weak and strong discontinuities at the newly created nodes (this information will later be used to compute the enrichment functions). As explained earlier in Section 2.2, determining the weights associated with strongly enriched DOFs relies on the discontinuities having a given orientation. As a result, integration elements would lay on either the *positive* or *negative* side of the crack, although this distinction is arbitrary and it is only important to keep consistency. In our implementation, given a point $\boldsymbol{p}$, we find its closest point along the crack $\boldsymbol{y}$, and we compute the sign $(\boldsymbol{n}_\mathrm{c} \cdot (\boldsymbol{p} - \boldsymbol{y}))$ to determine the region to which point $\boldsymbol{p}$ belongs.

Given the mesh element set $\mathcal{E}$ and assuming $|\mathcal{D}| \ll |\mathcal{E}|$ with $|\cdot|$ denoting set cardinality, the time complexity for the pseudo-code given in Algorithm 1 is $\mathcal{O}\,(|\mathcal{E}|)$. An efficient implementation would make use of a space decomposition technique to speedup discontinuity-element intersections. Choices of space decomposition techniques include, among others, tree data structures (binary space partition (BSP) trees, k-d trees, octrees) and grids.[31]

Integration All elements that do not interact with discontinuities are treated as in standard FEM. For integration elements, the computation of the local stiffness matrix and force vector is outlined in Algorithm 2.

As shown in the pseudo-code, integration is performed on the integration element following an isoparametric approach where the master element coordinate is denoted $\boldsymbol{\xi}$. At each Gauss quadrature point, the algorithm computes the shapes functions for the parent element and the enrichment functions, together with their derivatives. Therefore, the code given is split in a part that deals with the integration element and a part that deals with the parent mesh element. Once the functions and their derivatives are stacked into arrays, the contribution to the stiffness matrix and the force vector follows standard procedures.

It was mentioned earlier that one of the advantages of the formulation is to have a completely decoupled assembly of cohesive elements. For completeness, Algorithm 3 provides the assembly routine for cohesive elements.

It can be seen that the algorithm needs only information about the strong DOFs $\boldsymbol{\beta}_i$ and $\boldsymbol{\beta}_j$ associated with the end points of a cohesive element. It is shown that the orientation of the cohesive matrix is taken into account by using a rotation matrix and that a residual vector is also computed in case the cohesive law used is nonlinear.

Boundary conditions Imposing boundary conditions is as simple as in standard FEM. If a discontinuity intersects a Dirichlet boundary, as demonstrated in Examples 3.1 and 3.2, the corresponding DOFs can be readily prescribed after evaluating Equation (20).

Algorithm 2 Computation of local stiffness matrix and force vector for an integration element

---

Input: Integration element e_i with nodal coordinates $X = \begin{bmatrix} x_i & x_j & \dots \end{bmatrix}^\top$, parent e_p with co-ordinates X_p, constitutive matrix D, body force b, quadrature weights γ and coordinates ξ, enrichment weights w, number of local DOFs n

function GETLOCALARRAYS($e_i, X, e_p, X_p, D, b, \gamma, \xi, w, n$)

    $\{k, f\} \leftarrow \{0_{n \times n}, 0_{n \times 1}\}$ *– initialize data structures*

    – loop over integration points

    for $i \leftarrow 1, \dots, |\xi|$ **do**

        $\{F, F_{,x}\} \leftarrow \{[\,], [\,]\}$ *– initialize empty function arrays*

        – operations on the integration element

        $\{N, N_{,\xi}\} \leftarrow \text{lagrangian}\,(\xi_i, e_i)$ *– get Lagrangian functions/derivatives*

        $\{J^{-1}, j\} \leftarrow \text{jacobian}(X, N_{,\xi})$ *– get Jacobian inverse and determinant*

        for $k \leftarrow 1, \dots$ **do**   *– loop over enriched nodes*

            $w \equiv \{w_\psi, w_\chi\} \leftarrow \text{weights}\,(k)$ *– get weak and strong weights*

            $\{\psi_k, \psi_{k,\xi}, \chi_k, \chi_{k,\xi}\} \leftarrow \text{enrich}(N_k, N_{k,\xi}, w)$ *– get enrichments/derivatives*

            $\{\psi_{k,x}, \chi_{k,x}\} \leftarrow \{\psi_{k,\xi}\,J^{-1}, \chi_{k,\xi}\,J^{-1}\}$ *– derivatives w.r.t. global coordinates*

            $F \leftarrow \begin{bmatrix} F & \psi_k & \chi_k \end{bmatrix}$ *– stack enrichment functions*

            $F_{,x} \leftarrow \begin{bmatrix} F_{,x} & \psi_{k,x} & \chi_{k,x} \end{bmatrix}$ *– stack their derivatives*

        – operations on the parent

        $\xi_p \leftarrow \text{invert}(N\,X, e^p)$ *– invert global coordinate*

        $\{N_p, N_{p,\xi}\} \leftarrow \text{lagrangian}\,(\xi_p, e_p)$ *– get parent shape functions/derivatives*

        $J_p^{-1} \leftarrow \text{jacobian}(X_p, N_{p,\xi})$ *– get parent Jacobian inverse*

        $N_{p,x} \leftarrow N_{p,\xi}\,J_p^{-1}$ *– derivatives w.r.t. global coordinates*

        – gather all functions/derivatives and expand for multiple DOFs per node

        $N \leftarrow \text{expand}\left(\begin{bmatrix} F & N_p \end{bmatrix}\right)$ *– stack enrichments and shape functions*

        $B \leftarrow \text{expand}\left(\begin{bmatrix} F_{,x} & N_{p,x} \end{bmatrix}\right)$ *– stack their derivatives*

        – add contributions to stiffness matrix and residual vector

        $k \leftarrow k + \gamma_i\, j\, B^\top\, D\, B$ *– update stiffness matrix*

        $f \leftarrow f + \gamma_i\, j\, N^\top\, b|_{N X}$ *– update force vector*

    return k, f

In Section 3.1, we demonstrated a case where a natural boundary condition is prescribed at one of the edges that intersects the crack. We showed how a jump in the BC values can be readily taken into consideration by splitting the boundary integral into two parts at either side of the crack. The pseudo-code for this case is omitted because it would be similar to that given in Algorithm 2, with the main differences being *(i)* integration is performed over 1-D elements; *(ii)* there is no need to compute derivatives; and *(iii)* only a contribution to the force vector is needed.

Post-processing As mentioned earlier, nodes of the original mesh conserve the Kronecker property, and thus post-processing is only needed if a better representation of the displacement field is required, *e.g.*, for visualizing the crack opening. Note that even the displacement jump at nodes along the discontinuity can be obtained without requiring a post-processing stage.

The pseudo-code for the post-processing procedure is listed in Algorithm 4. The main loop over integration elements is performed to change the connectivity table of those elements that reside on one side of the crack. The displacement field is computed at both sides of the crack through Equation (20), and the global displacement vector U is modified accordingly. The data structures in the algorithm with a $\pm$ subscript imply two sets (both sides of the crack). Implicit in the algorithm is the fact that enriched nodes are visited once. Since nodes of the original mesh keep their values, no further modification is required there.

Algorithm 3 Cohesive element local stiffness matrix and force vector

---

Input: Cohesive element c_i with nodal coordinates $\begin{bmatrix} \boldsymbol{x}_i & \boldsymbol{x}_j \end{bmatrix}^\mathsf{T}$, quadrature arrays $\{\boldsymbol{\gamma}, \boldsymbol{\xi}\}$, strong
enriched DOFs $\boldsymbol{\beta} = \begin{bmatrix} \boldsymbol{\beta}_i & \boldsymbol{\beta}_j \end{bmatrix}^\mathsf{T}$

function GETLOCALARRAYS$(c_i, \boldsymbol{X}, \boldsymbol{\beta}, \boldsymbol{\gamma}, \boldsymbol{\xi})$
    $\{k_\mathrm{n}, k_\mathrm{t}\} \leftarrow \mathrm{spring}(c_i)$ *– get cohesive spring constants*
    $\boldsymbol{A} \leftarrow \begin{bmatrix} k_\mathrm{n} & 0 \\ 0 & k_\mathrm{t} \end{bmatrix}$ *– cohesive constants matrix*
    $n \leftarrow |\boldsymbol{\beta}|$ *– get number of local DOFs*
    $\{\boldsymbol{k}, \boldsymbol{r}\} \leftarrow \{\boldsymbol{0}_{n \times n}, \boldsymbol{0}_{n \times 1}\}$ *– initialize data structures*
    – loop over integration points
    for $i \leftarrow 1, \ldots, |\boldsymbol{\xi}|$ **do**
        $\{\boldsymbol{N}, \boldsymbol{N}_{,\xi}\} \leftarrow \mathrm{lagrangian}\,(\boldsymbol{\xi}_i, c_i)$ *– get Lagrangian functions/derivatives*
        $j \leftarrow \mathrm{jacobian}(\boldsymbol{X}, \boldsymbol{N}_{,\xi})$ *– obtain Jacobian*
        $\boldsymbol{N} \leftarrow \mathrm{expand}(\boldsymbol{N})$ *– expand for multiple DOFs per node*
        $\delta \leftarrow \boldsymbol{N}\boldsymbol{\beta}$ *– compute displacement jump*
        – compute transformation matrices
        $\boldsymbol{R} \leftarrow \mathrm{rotation}(c_i)$ *– compute rotation matrix*
        $\boldsymbol{Q} \leftarrow \boldsymbol{R}\boldsymbol{N}$
        – add contributions to stiffness matrix and residual vector
        $\boldsymbol{t}_\mathrm{c} \leftarrow \boldsymbol{R}^\mathsf{T}\boldsymbol{A}\delta$ *– get cohesive traction*
        $\boldsymbol{k} \leftarrow \boldsymbol{k} + \gamma_i\, j\, \boldsymbol{Q}^\mathsf{T}\, \boldsymbol{A}\, \boldsymbol{Q}$ *– update stiffness matrix*
        $\boldsymbol{r} \leftarrow \boldsymbol{r} - \gamma_i\, j\, \boldsymbol{N}^\mathsf{T}\, \boldsymbol{t}_\mathrm{c}$ *– update residual vector*
    return $\boldsymbol{k}, \boldsymbol{r}$

APPENDIX B: ELEMENT ARRAYS FOR A ONE-DIMENSIONAL X/GFEM ELEMENT WITH DISCONTINUOUS ENRICHMENT

We report the expression of the relation $\boldsymbol{KU} = \boldsymbol{F}$ for the 1-D bar of Figure 1 using a two-node X/GFEM element enriched with the Heaviside step function Equation (14). This enriched element has four DOFs, two per node, labeled with $\hat{u}$ (standard) and $\tilde{u}$ (enriched). With reference to the displacement contribution to the discretized weak formulation of the governing equations described by Simone *et al.*,[32] and without considering the nonlinear part (damage is therefore excluded), the relation $\boldsymbol{KU} = \boldsymbol{F}$ reads

$$\begin{bmatrix} k_{\hat{u}\hat{u}} & k_{\hat{u}\tilde{u}} \\ k_{\tilde{u}\hat{u}} & k_{\tilde{u}\tilde{u}} \end{bmatrix} \begin{bmatrix} \hat{u} \\ \tilde{u} \end{bmatrix} = \begin{bmatrix} f_{\hat{u}} \\ f_{\tilde{u}} \end{bmatrix}. \tag{B1}$$

The entries in the stiffness matrix are computed according to

$$\boldsymbol{k}_{\hat{u}\hat{u}} = \int_0^{x_\Gamma} E_\mathrm{I} A\, \boldsymbol{B}^\mathsf{T}\boldsymbol{B}\ \mathrm{d}x + \int_{x_\Gamma}^L E_\mathrm{II} A\, \boldsymbol{B}^\mathsf{T}\boldsymbol{B}\ \mathrm{d}x = \frac{A\,(E_\mathrm{II} - w[\![E]\!])}{L} \begin{bmatrix} 1 & -1 \\ -1 & 1 \end{bmatrix}, \tag{B2a}$$

$$\boldsymbol{k}_{\tilde{u}\hat{u}} = \boldsymbol{k}_{\hat{u}\tilde{u}} = \int_{x_\Gamma}^L E_\mathrm{II} A\, \boldsymbol{B}^\mathsf{T}\boldsymbol{B}\ \mathrm{d}x = \frac{A E_\mathrm{II}\,(1 - w)}{L} \begin{bmatrix} 1 & -1 \\ -1 & 1 \end{bmatrix}, \tag{B2b}$$

$$\boldsymbol{k}_{\tilde{u}\tilde{u}} = \int_{x_\Gamma}^L E_\mathrm{II} A\, \boldsymbol{B}^\mathsf{T}\boldsymbol{B}\ \mathrm{d}x + (\boldsymbol{N}^\mathsf{T} k \boldsymbol{N})|_{x_\Gamma} = \frac{A E_\mathrm{II}(1 - w)}{L} \begin{bmatrix} 1 & -1 \\ -1 & 1 \end{bmatrix} + k \begin{bmatrix} (1-w)^2 & (1-w)w \\ (1-w)w & w^2 \end{bmatrix}, \tag{B2c}$$

where $\boldsymbol{N}$ is a matrix containing one-dimensional linear shape functions, $\boldsymbol{B}$ is a matrix containing derivatives of these shape functions, and the surface integral has been computed by evaluating the integrand at $x = x_\Gamma$, the discontinuity location. The final expression of the stiffness is given in Equation (15).

The boundary condition at the clamped end ($u(0) = 0$) poses a constrain only on the standard DOF $\hat{u}_1$ ($\hat{u}_1 = 0$) as it can be easily determined by expanding the X/GFEM approximation in Simone *et al.*[32], Equation (4).

Algorithm 4 Post-process

Input: Solution vector U, mesh $\mathcal{M} := \{\mathcal{N}, \mathcal{E}\}$, and enrichment weights w

    function POSTPROCESS($U, \mathcal{M}, w$)
        – loop over integration elements ($\mathcal{E}_e \quad \mathcal{E}$)
        for $e_i \in \mathcal{E}_e$ **do**
            $e_p \leftarrow \mathrm{parent}(e_i)$ *– parent element*
            $[u, \alpha, \beta] \leftarrow \mathrm{localize}(e_i, e_p, U)$ *– element local DOFs*
            for $k \leftarrow 1, \ldots$ **do**   *– loop over enriched nodes*
                – operations on the integration element
                $X \leftarrow \begin{bmatrix} x_i & \ldots \end{bmatrix}^{\mathsf{T}}$ *– integration element coordinates*
                $\xi_k \leftarrow \mathrm{invert}(x_k, e_i)$ *– master element coordinate*
                $N_k \leftarrow \mathrm{lagrangian}\left(\xi_k, e_i\right)$ *– Lagrangian functions*
                $w \leftarrow \mathrm{weights}\,(k)$ *– weak and strong weights*
                $\left\{\psi_k, \chi_k\right\}_{\pm} \leftarrow \mathrm{enrich}(N_k, w)$ *– weak and strong enrichments*
                – operations on the parent element
                $\xi_p \leftarrow \mathrm{invert}(x_k, e_p)$ *– master coordinate*
                $N_p \leftarrow \mathrm{lagrangian}\left(\xi_p, e_p\right)$ *– parent shape functions*
                – compute displacement at both sides of the crack
                $N_{\pm} \leftarrow \begin{bmatrix} N_p & \psi_k & \chi_k \end{bmatrix}_{\pm}$ *– stack functions*
                $u_{\pm} \leftarrow N_{\pm} \begin{bmatrix} u & \alpha & \beta \end{bmatrix}^{\mathsf{T}}$ *– compute displacement*
                $U \leftarrow \mathrm{modify}(u_{\pm}, U)$ *– modify solution vector*
            – modify connectivity if integration element lies on the positive side
        if positiveSide(e_i) **then**
            $e_i \leftarrow \mathrm{reconnect}(e_i, \mathcal{N})$
    return $U, \mathcal{M}$

As for the natural boundary conditions, they are directly enforced in F through

$$f_{\hat{u}} = \int_{\Gamma_t} N^{\mathsf{T}} \bar{t} \ \mathrm{d}\Gamma \quad \text{and} \tag{B3a}$$

$$f_{\tilde{u}} = \int_{\Gamma_t^+} N^{\mathsf{T}} \bar{t} \ \mathrm{d}\Gamma, \tag{B3b}$$

where Γ_t^+ is the part of the boundary where prescribed tractions $\bar{t}$ are applied with the enrichment function different from zero. With reference to the 1-D problem in Section 2.1, there is an unknown force R at the clamped end that in principle should be added to both DOFs active at $x = 0$. However, since the enrichment function is zero at that location, only the entry corresponding to $\hat{u}_1$ is filled with R, see Equation (B3a). Analogous considerations hold for the concentrated force of intensity P at $x = L$: since the enrichment function is equal to one at $x = L$, both DOF entries are filled with P. The right-hand side of the full system is given in Equation (16).

APPENDIX C: ASYMPTOTIC FIELDS

For completeness, we provide the expressions of the displacement and stress fields in the vicinity of a crack due to a remote tensile stress:

$$u_K = \begin{cases} \dfrac{K_{\mathrm{I}}}{4G} \sqrt{\dfrac{r}{2\pi}} \begin{bmatrix} (2\kappa - 1)\cos\frac{\theta}{2} - \cos\frac{3\theta}{2} \\ (2\kappa + 1)\sin\frac{\theta}{2} - \sin\frac{3\theta}{2} \end{bmatrix} & \text{for mode I,} \\[4mm] \dfrac{K_{\mathrm{II}}}{4G} \sqrt{\dfrac{r}{2\pi}} \begin{bmatrix} (2\kappa + 3)\sin\frac{\theta}{2} + \sin\frac{3\theta}{2} \\ (3 - 2\kappa)\cos\frac{\theta}{2} - \cos\frac{3\theta}{2} \end{bmatrix} & \text{for mode II.} \end{cases}$$

$$\tag{C1a}$$
$$\tag{C1b}$$

In Equation (C1a) and (C1b), r and θ are the polar coordinates from the crack tip, G is the shear modulus of the material, and κ is Kosolov's constant given by

$$\kappa = \begin{cases} 3 - 4\nu & \text{for plane strain,} \\ \dfrac{3 - \nu}{1 + \nu} & \text{for plane stress.} \end{cases} \tag{C2}$$

The stress (in Voigt's notation) is given by

$$\sigma_K = \begin{cases} \dfrac{K_\mathrm{I}}{\sqrt{2\pi r}} \cos \dfrac{\theta}{2} \begin{bmatrix} 1 - \sin \frac{\theta}{2} \sin \frac{3\theta}{2} \\ 1 + \sin \frac{\theta}{2} \sin \frac{3\theta}{2} \\ \sin \frac{\theta}{2} \cos \frac{3\theta}{2} \end{bmatrix} & \text{for mode I,} \tag{C3a} \\[2em] \dfrac{K_\mathrm{II}}{\sqrt{2\pi r}} \begin{bmatrix} - \sin \frac{\theta}{2} \left(2 + \cos \frac{\theta}{2} \cos \frac{3\theta}{2} \right) \\ \sin \frac{\theta}{2} \cos \frac{\theta}{2} \cos \frac{3\theta}{2} \\ \cos \frac{\theta}{2} \left(1 - \sin \frac{\theta}{2} \sin \frac{3\theta}{2} \right) \end{bmatrix} & \text{for mode II.} \tag{C3b} \end{cases}$$

APPENDIX D: COMPUTATION OF WEIGHTS FOR A TRIANGULAR ELEMENT

In this section, we list the *Mathematica*® code that computes the weights for the triangle in Figure 5. The code creates an interactive manipulation environment where the location of the triangle vertices and the points that define the discontinuity can be moved, and results are computed in real time. The code is not optimized for speed and does not constrain the line-to-line intersections. Yet it can be used to understand through dynamic manipulation how the weights of the discontinuous enrichment functions are computed.

```
In[1]:= (* Shape functions *)
        At[X_] := 1/2 Det[( {
          {1, X[[1, 1]], X[[1, 2]]},
          {1, X[[2, 1]], X[[2, 2]]},
          {1, X[[3, 1]], X[[3, 2]]}
          })]
        N1t[x_, y_, X_] := (1/(2 At[X]))(X[[2, 1]] X[[3, 2]] - X[[3, 1]] X[[2, 2]] +
          (X[[2, 2]] - X[[3, 2]]) x + (X[[3, 1]] - X[[2, 1]]) y)
        N2t[x_, y_, X_] := (1/(2 At[X]))(X[[3, 1]] X[[1, 2]] - X[[1, 1]] X[[3, 2]] +
          (X[[3, 2]] - X[[1, 2]]) x + (X[[1, 1]] - X[[3, 1]]) y)
        N3t[x_, y_, X_] := (1/(2 At[X]))(X[[1, 1]] X[[2, 2]] - X[[2, 1]] X[[1, 2]] +
          (X[[1, 2]] - X[[2, 2]]) x + (X[[2, 1]] - X[[1, 1]]) y)
In[2]:= (* Intersection between two lines *)
        intersect[{p1x_, p1y_}, {p2x_, p2y_}, {q1x_, q1y_}, {q2x_, q2y_}] :=
        With[{d1 = Det[({{p1x, p1y}, {p2x, p2y}})],
             d2 = Det[({{q1x, q1y}, {q2x, q2y}})],
             d3 = Det[({{p1x - p2x, p1y - p2y}, {q1x - q2x, q1y - q2y}})]},
             (* Compute {x,y} coordinates for intersection point *)
             {
              Det[({{d1, p1x - p2x}, {d2, q1x - q2x}})]/d3, (* x *)
              Det[({{d1, p1y - p2y}, {d2, q1y - q2y}})]/d3  (* y *)
             }
            ]
In[3]:= Manipulate[
        DynamicModule[{m = (l2[[2]] - l1[[2]])/(l2[[1]] - l1[[1]]), pi, pj,
          wi, wj},

          (* Find intersection points *)
          pi = {pix, piy} = intersect[p1, p3, l1, l2];
          pj = {pjx, pjy} = intersect[p2, p3, l1, l2];
```

```
(* Compute weight equations *)
Wi1eq = Simplify[wi1 N2t[pix, piy, {p3, pi, pj}]] ==
   -Simplify[N3t[pix, piy, {p1, p2, p3}]];
Wi2eq = Simplify[wi2 N3t[pix, piy, {p1, pj, pi}]] ==
    Simplify[N1t[pix, piy, {p1, p2, p3}]];
Wj1eq = Simplify[wj1 N3t[pjx, pjy, {p3, pi, pj}]] ==
   -Simplify[N3t[pjx, pjy, {p1, p2, p3}]];
Wj2eq = Simplify[wj2 N3t[pjx, pjy, {p1, p2, pj}]] ==
    Simplify[N2t[pjx, pjy, {p1, p2, p3}]];

wi = -Wi1eq[[2]];
wj = -Wj1eq[[2]];

(* Plots for first enrichment function *)
gi1 = Plot3D[-wi*N2t[x, y, {p3, pi, pj}], {x, y} \[Element]
   Polygon[{p3, pi, pj}]];
gi2 = Plot3D[(1 - wi)*N3t[x, y, {p1, pj, pi}] , {x, y} \[Element]
   Polygon[{p1, pj, pi}]];

(* Plots for second enrichment function *)
gj1 = Plot3D[-wj*N3t[x, y, {p3, pi, pj}], {x, y} \[Element]
   Polygon[{p3, pi, pj}]];
gj2 = Plot3D[(1 - wj)*N3t[x, y, {p1, p2, pj}] , {x, y} \[Element]
   Polygon[{p1, p2, pj}]];
gj3 = Plot3D[(1 - wj)*N2t[x, y, {p1, pj, pi}] , {x, y} \[Element]
   Polygon[{p1, pj, pi}]];

(* Plots for the enrichment function *)
f1 = Plot3D[-wi*N2t[x, y, {p3, pi, pj}] -
   wj*N3t[x, y, {p3, pi, pj}], {x, y} \[Element]
   Polygon[{pi, pj, p3}]];
f2 = Plot3D[(1 - wi)*N3t[x, y, {p1, pj, pi}] + (1 - wj)*
   N2t[x, y, {p1, pj, pi}], {x, y} \[Element]
  Polygon[{p1, pj, pi}]];
f3 = Plot3D[(1 - wj)*N3t[x, y, {p1, p2, pj}], {x, y} \[Element]
   Polygon[{p1, p2, pj}]];

(* Output first column *)
Row[{Column[{
   Plot[m (x - l1[[1]]) + l1[[2]], {x, 0, 1},
    Axes -> None,
    ImageSize -> Medium,
    Epilog -> {Thick, PointSize[0.05],
      {Line[{p1, p2, p3, p1}],
       Line[{p1, p2, pj, p1}],
       Line[{p3, pi, pj, p3}],
       {Red, Point[pi]},
       {Red, Point[pj]}
       }
      },
    PlotRange -> {{-1/2, 3/2}, {-0.1, 1.1}},
    AspectRatio -> Automatic],

   (* Node i *)
   Style["\nNode i", Bold, FontSize -> 14],
   Row[{Style["pi = ", Bold], pi}],
   Row[{Style["wi1,wi2 = ", Bold], {Wi1eq[[2]], Wi2eq[[2]]}}],
   Row[{Style["wi = ", Bold], wi}],
   Row[{Style["check: 1 - wi = wi2:", Bold], 1 - wi}],

   (* Node j *)
   Style["\nNode j", Bold, FontSize -> 14],
   Row[{Style["pj = ", Bold], pj}],
   Row[{Style["wj1,wj2 = ", Bold], {Wj1eq[[2]], Wj2eq[[2]]}}],
```

```
      Row[{Style["wj = ", Bold], wj}],
      Row[{Style["check: 1 - wj = wj2: ", Bold], 1 - wj}]
      }],

   (* Second column, firt enrichment *)
   Column[{
     Show[gi1, gi2,
      PlotLabel -> Style[Subscript[\[CapitalPsi], i], Large],
      ImageSize -> Medium, PlotRange -> Automatic,
      ViewPoint -> {1, Pi/2, 2}]
     }],
   (* Third column, second enrichment *)
   Column[{
     Show[gj1, gj2, gj3,
      PlotLabel -> Style[Subscript[\[CapitalPsi], j], Large],
      ImageSize -> Medium, PlotRange -> Automatic,
      ViewPoint -> {1, Pi/2, 2}]
     }],
   (* Fourth column, sum of enrichments *)
   Column[{
     Show[f1, f2, f3,
      PlotLabel ->
       Style[Subscript[\[CapitalPsi], i] + Subscript[\[CapitalPsi],
          j], Large], ImageSize -> Medium, PlotRange -> All,
      ViewPoint -> {1, Pi/2, 2}]
     }]
    }]
  ],
 {{p1, {0, 0}}, Locator},
 {{p2, {1, 0}}, Locator},
 {{p3, {0.5, 1}}, Locator},
         {{l1, {-0.1, 1/2}}, Locator},
         {{l2, {1.1, 1/2}}, Locator}]
```
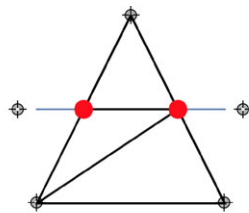
Out[3]=

Node i
$p_i = \{0.25, 0.5\}$
$w_{i1}, w_{i2} = \{-0.5, 0.5\}$
$w_i = 0.5$
check: $1 - w_i = w_{i2}$: 0.5

Node j
$p_j = \{0.75, 0.5\}$
$w_{j1}, w_{j2} = \{-0.5, 0.5\}$
$w_j = 0.5$
check: $1 - w_j = w_{j2}$: 0.5